ACS OMEGA

Open Access

http://pubs.acs.org/journal/acsodf

Article

Multifaceted Study of a Y-Shaped Pyrimidine Compound: Assessing Structural Properties, Docking Interactions, and Third-Order Nonlinear Optics

Krishna Murthy Potla,* Poojith Nuthalapati, Jahnavi Thokala Sasi Mohan, Francisco A. P. Osório, Clodoaldo Valverde,* Suneetha Vankayalapati, Suchetan Parameshwar Adimule, Sanja J. Armaković, Stevan Armaković, and Y. Sheena Mary

Cite This: *ACS Omega* 2024, 9, 7424−7438

Read Online

ACCESS | Metrics & More | Article Recommendations | Supporting Information

ABSTRACT: In this study, we report the synthesis of a new compound, *N*4,*N*4-dimethyl-2-(methylsulfanyl)-*N*6-(4-phenoxyphenyl)pyrimidine-4,6-diamine (DMS), and its comprehensive analysis through structural and spectroscopic characterizations, reactivity parameters, and nonlinear optical properties, utilizing a combination of experimental and computational techniques. The experimental aspect of the investigation encompassed structural characterization using X-ray diffraction and spectroscopic assessments employing Fourier-transform infrared, Raman, and nuclear magnetic resonance techniques, along with thermal analysis. Our computational approach involved density functional theory (DFT) calculations and molecular dynamics (MD) simulations to examine the local reactivity properties of DMS. We employed fundamental reactivity descriptors to evaluate DMS's local reactivity and utilized MD simulations to identify DMS atoms engaging in significant interactions with water molecules. We conducted periodic DFT calculations on DMS's crystal structure to investigate the contributions of specific atoms and groups to the compound's overall stability as well as to analyze noncovalent interactions between DMS molecules. We assessed the nonlinear optical properties through dynamic second hyperpolarizability and third-order nonlinear susceptibility calculations. Additionally, we conducted a comparative analysis of the static and dynamic second hyperpolarizability for the DMS molecule within the sum-over-states framework. The obtained value for the third-order nonlinear susceptibility, $\chi^3 = 65.41 \times 10^{-20}$ m^2/V^2 (λ = 1907 nm), exceeds those of other organic materials reported in previous studies, indicating that the DMS crystal holds promise as a nonlinear optical material for potential application in photonic device fabrication. Furthermore, molecular docking studies were performed with the 3E5A, 4EUT, and 4EUU proteins, yielding binding affinities of −8.1, −8.2, and −8.3 kcal/mol, respectively, in association with the ligand.

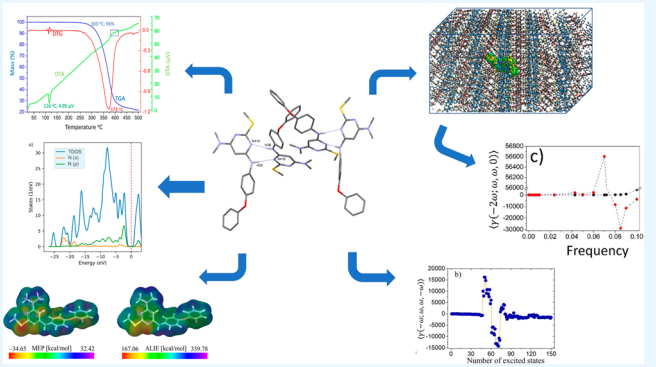

1. INTRODUCTION

Nonlinear optical (NLO) materials have attracted more attention due to their wide range of applications in storage, optoelectronics, sensors, optical data processing, semiconductors, photonic, ferroelectric, and superconductor devices.[1−4] Compared to inorganic materials, organic molecules receive considerable attention from researchers due to their architectural flexibility and easy and low-cost synthesis to achieve an optimum NLO response.

An extensive literature survey on various nonlinear optical and optoelectronic properties of pyrimidine-based molecules emphasizes their outstanding potential for practical applications in science and technology. Pyrimidines, with their notable electron-withdrawing character and significant aromaticity, are essential in the creation of novel organic chromophores for nonlinear optical materials. These highly π deficient aromatic heterocycles have inherent coplanarity that facilitates the formation of push−pull molecules, impacting luminescence properties.[5] They offer further applications through their nitrogen atoms, enabling the development of supramolecular assemblies and sensor systems via protonation and hydrogen bonding. The NLO properties of specific dyes consisting of electron-deficient pyrimidine core and γ-

Received: June 20, 2023
Revised: November 17, 2023
Accepted: November 23, 2023
Published: February 6, 2024

methylenepyrans as terminal donor (D) groups have been investigated in a study by Achelle et al.[6] Their study consisted of both experiments and density functional theory (DFT) calculations and has demonstrated that curtail structural parameters affect the NLO sensitivity of these dyes. Probably the strongest motivation to study NLO and optoelectronic properties of our newly synthesized pyrimidine-based molecule we found in the review by Feckova et al.[7] Namely, their study covered a huge library of NLO chromophores based on a pyrimidine scaffold. Additionally, pyrimidines contribute to the structure of two-photon absorption (TPA) chromophores, especially the 4,6-di(arylvinyl)pyrimidines, and are also incorporated into quadratic Nonlinear Optical (NLO) chromophores. Numerous pyrimidine derivatives demonstrating Intramolecular Charge Transfer (ICT) have been investigated over the past decade, with a specific focus on the synthesis and NLO response of 4-(arylvinyl)pyrimidines.[8,9] These compounds have recently been the subject of theoretical NLO studies by an independent research team.[7] Meanwhile, pyrimidines denote one of the most prevalent heterocyclic compounds found in alkaloids and nucleic bases and exhibit remarkable pharmacological activities, including anti-HIV,[10] antiviral,[11] antitubercular,[12] anticancer,[13] antimicrobial,[14] antihypertensive,[15] anti-inflammatory,[16] antiplasmodial,[17] and anticonvulsant.[18] The ability to finely tune pyrimidine-based molecules has been used in the creation of covalent organic frameworks (COFs), which are of interest due to their crystallinity, porosity, and tunability. The optoelectronic properties of these molecules contribute to light-induced hydrogen evolution, a process that holds promise as a sustainable source of carbon-free energy.[19]

Numerous experimental methods facilitate the synthesis and analysis of molecules; however, conducting comprehensive investigations of newly synthesized molecules can be difficult and costly. The swift advancements in computational techniques now allow for complementary characterization studies, yielding results closely tied to structural, reactive, and other critical properties. This amalgamation of experimental and theoretical approaches not only enables in-depth molecular examinations but also accelerates the overall research process. Computational investigations have proven invaluable and are routinely employed in industries such as pharmaceuticals and materials science. A vast number of papers exist where computational analysis was helpful for pharmaceutical and materials science industries.[20−26]

In conclusion, the study of the nonlinear optical and optoelectronic properties of pyrimidine-based molecules is motivated by their potential applications in various scientific and technological fields, ranging from energy production to medical applications. The synthesis of new pyrimidine molecules presents an opportunity to further understand and exploit their NLO and optoelectronic properties. This study aims to contribute to this growing body of knowledge by investigating the NLO and optoelectronic properties of a newly synthesized pyrimidine molecule. Through this research, we hope to not only expand our understanding of pyrimidine-based molecules but also pave the way for the development of more efficient and versatile optoelectronic devices.

All of these facts motivated us to synthesize a new pyrimidine derivative, *N*4,*N*4-dimethyl-2-(methylsulfanyl)-*N*6-(4-phenoxyphenyl)pyrimidine-4,6-diamine (DMS). Several experimental and computational tools have been used in its thorough study, and the readers will become familiar with them as they read the manuscript.

2. EXPERIMENTAL AND THEORETICAL METHODS

In this section, we provide a thorough analysis of the research procedures, discussing its objectives, background, and the synthesis of DMS. We explore X-ray crystallography, the reactive properties of DMS, Hirshfeld surface analysis, and density of states (DOS) analysis. The focus then shifts to the nonlinear optical properties of the DMS crystal, its potential applications, and the sum-over-states (SOS) approach.

2.1. General Remarks. The reagents and solvents used in this study were of AnalaR grade and were procured from commercial sources. The synthesis was performed under anaerobic (inert atmosphere) conditions. The Fourier-transform infrared (FT-IR) spectrum was recorded on a PerkinElmer Spectrum1 FT-IR Spectrometer in the form of KBr disc in the range 4000−450 cm^{-1}, with 1.0 cm^{-1} spectral resolution (Figure S1). The Fourier-transform (FT) Raman spectrum was recorded on a Bruker RFS 27: Standalone FT-Raman Spectrometer in the range 50−4000 cm^{-1}, with 2.0 cm^{-1} spectral resolution and Nd:YAG 1064 nm laser source (Figure S2). ^{1}H NMR (Figure S3) and ^{13}C $\{^{1}H\}$ NMR (Figure S4) spectra were recorded on a Bruker AMX-400 MHz spectrometer operating at room temperature in deuterated dimethyl sulfoxide (DMSO-d_6) as the solvent. The chemical shift values (δ) are reported in parts per million (ppm) using tetramethylsilane (TMS) as an internal standard. The thermal analysis of the DMS sample was performed by using an EXSTAR TG/DTA 6300 instrument.

2.2. Synthesis of DMS. We dissolved 6-chloro-*N*,*N*-dimethyl-2-(methylsulfanyl)-pyrimidin-4-amine (0.5 g, 2.46 mmol) and 4-phenoxyaniline (0.68 g, 3.69 mmol) in 1-butanol (15 mL). To this mixture was added triethylamine (2.4 mL, 2.95 mmol) dropwise and then refluxed for 12 h. After the completion of the reaction as indicated by thin-layer chromatography (TLC), the reaction mass was evaporated under reduced pressure and purified by column chromatography. The compound was dissolved in methanol and allowed to evaporate at room temperature. Needle-shaped crystals of *N*4,*N*4-dimethyl-2-(methylsulfanyl)-*N*6-(4-phenoxyphenyl)-pyrimidine-4,6-diamine (0.57 g, yield: 66%) were obtained after 4−5 days (Scheme 1).

Scheme 1. Synthetic Scheme for *N*4,*N*4-Dimethyl-2-(methylsulfanyl)-*N*6-(4-phenoxyphenyl)pyrimidine-4,6-diamine

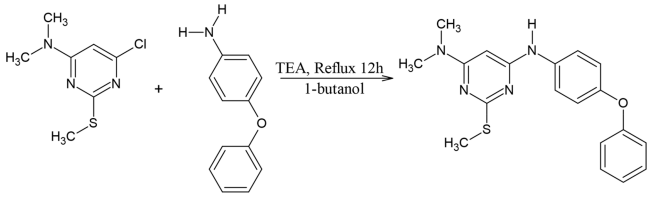

^{1}H NMR (400 MHz, DMSO-d_6) δ, ppm: 2.85 (s, 3H), 2.98 (s, 6H), 5.75 (s, 1H), 6.98 (m, 4H), 7.09 (t, 1H), 7.36 (t, 2H), 7.59 (d, 2H), 9.42 (s, 1H).

^{13}C NMR (400 MHz, DMSO-d_6) δ, ppm: 13.31, 36.58, 79.11, 117.67, 119.53, 121.06, 122.71, 129.85, 136.69, 150.46, 157.65, 160.33, 162.01, 168.90.

https://doi.org/10.1021/acsomega.3c04380
ACS Omega 2024, 9, 7424−7438

2.3. X-ray Crystallography Details. A colorless, needle-shaped single crystal of the title compound, with dimensions 0.3 mm × 0.25 mm × 0.2 mm, was selected and mounted on a Bruker APEX-II CCD diffractometer with monochromatic Mo Kα radiation (λ = 0.71073 Å) at 296(2) K. The data were processed with SAINT and absorption corrected using SADABS.[27] The structure was solved by the direct method using the program SHELXL[28] and was refined by full-matrix least-squares techniques on F^2 using anisotropic displacement parameters for all non-hydrogen atoms. The carbon-bound hydrogen atoms were positioned with idealized geometry by using a riding model with C−H = 0.93 Å (for C_{arm}−H) and 0.96 Å (for C_{methyl}−H). H atoms were refined with isotropic displacement parameters (set to 1.2−1.5 times the U_{eq} of the parent atom). The nitrogen-bound H atoms were also positioned geometrically using a riding model with N−H = 0.86 Å.

2.4. Molecular Reactive Properties and Docking Studies of DMS. Schrödinger Materials Science Suite 2022−4 (SMSS) has been used for the computational analysis of reactive properties of the title molecule based on combined DFT calculations and molecular dynamics (MD) simulations. The Jaguar[29] program was used for DFT calculations, while the Desmond[30−33] program was used for MD simulation. The Maestro[34] program was used for the preparation of input files and visualization of results.

DFT calculations with the Jaguar program have been performed with the B3LYP functional with the 6-311++G(d,p) basis set to calculate the molecular electrostatic potential (MEP) and average local ionization energy (ALIE) surfaces. The same functional was used for calculations of bond dissociation energies for hydrogen abstraction (H-BDE). The Desmond program for MD simulations was used with the extended OPLS3 (OPLS3e)[30,35−37] force field. The simulation time of 10 ns was used, while other parameters included a temperature of 300 K, pressure of 1.0325 bar, and cutoff radius of 10 Å. The MD simulation system was of NPT ensemble type, meaning that pressure and temperature were kept constant and contained one DMS molecule surrounded by water (∼2500 molecules) in a cubic simulation box. The solvent effects in MD simulation were regulated by the simple point charge (SPC) model.[38]

Optimizations at the molecular DFT level were preceded by preoptimization with the semiempirical method GFN2-xTB, developed by Prof. Grimme and co-workers.[39−41] GFN2-xTB calculations were performed using the online xtb calculator available at https://atomistica.online.[42]

The molecular docking simulations were performed by AutoDock 4.2 software[43] with 3E5A, 4EUT, and 4EUU proteins.

2.5. Hirshfeld Surface Analysis. The three-dimensional Hirshfeld Surface (HS) maps and the two-dimensional fingerprint (FP) depictions were generated by using the CrystalExplorer17 program.[44] The surfaces have been mapped over d_{norm} (1), *shape index* (2), *curvedness* (3), and *fragment path* (4) in the range of −0.4929 (red) − 1.5032 Å (blue), − 1.0 (concave) − 1.0 Å (convex), − 4.0 (flat) − 0.4 Å (singular), and 0−29 au, respectively (Figure S5). The d_{norm} surface evaluates the distances from the surface to the exterior nearest atom (d_e) and the nearest atom internal to surface (d_i) normalizing them as a function of the van der Waals radius. The FP is presented in the expanded view, with the distances d_e and d_i in the range 0.6−2.8 Å presented on the graph axes. The hydrogen bond lengths were immediately modified to regular standard neutron values, i.e., C−H = 1.083 Å and N−H = 1.009 Å, when the cif file was uploaded into the CrystalExplorer17 software.

2.6. Density of States (DOS). Periodic DFT calculations have been performed with the Quantum Espresso program,[45,46] as incorporated in Schrödinger Materials Science Suite (SMSS). These calculations have been performed with the PBE[47] functional and ultrasoft pseudopotentials, using the crystal structure that was previously experimentally determined.

2.7. Nonlinear Optical Properties of DMS Crystal. The Supermolecule (SM) method was used to simulate the polarization effect of the crystalline environment on a single DMS molecule. This approach has proven to be effective in studying the optical properties of organic materials, providing theoretical results that align with experimental data. A total of 5832 molecules comprising 262,440 atoms were used to mimic the crystalline environment. In this method, surrounding molecules are treated as point charges, beginning with the calculation of partial atomic charges using the MP2/6-311+G(d) and CHELPG schemes.[48−50] The process involves the iterative replacement of surrounding molecules with CHELPG partial charges, followed by calculation of the electric dipole moment and a new set of partial charges.[48,51−61] The process is repeated until the electric dipole moment of the embedded molecule converges (μ = 12.04D or 4.02 × 10^{-29} Cm). Figure 1 demonstrates this convergence, with step 0 representing the isolated molecule (μ = 5.22D or 1.74 × 10^{-29} Cm) and subsequent steps showing the embedded molecule within the crystal. The simulated bulk representation is also provided.

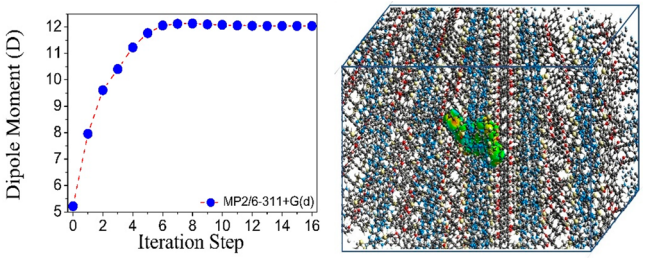

Figure 1. (a) Convergence of the dipole moment of the embedded molecule of DMS. (b) Schematic representation of the bulk highlighting the symmetric unit (in green) in the center.

In the present work, the electric dipole moment (μ and the average linear polarizability ($\langle\alpha\rangle$) have been calculated through the following expressions.

$$\mu = (\mu_x^2 + \mu_y^2 + \mu_z^2)^{1/2} \quad (1)$$

$$\langle\alpha(-\omega;\ \omega)\rangle = \frac{\alpha_{xx}(-\omega;\ \omega) + \alpha_{yy}(-\omega;\ \omega) + \alpha_{zz}(-\omega;\ \omega)}{3} \quad (2)$$

In the context of third-order Nonlinear Optical (NLO) responses, three specific reactions are recognized, each denoted by their respective expressions. The static response is represented by $\gamma(0;0;0;0)$, the Electro-Optical Pockels Effect (EOPE) by $\gamma(-\omega;\omega;0;0)$, and the Electric Field-Induced Second Harmonic Generation (EFSHG) by $\gamma(-2\omega;\omega;\omega;0)$.

https://doi.org/10.1021/acsomega.3c04380
ACS Omega 2024, 9, 7424−7438

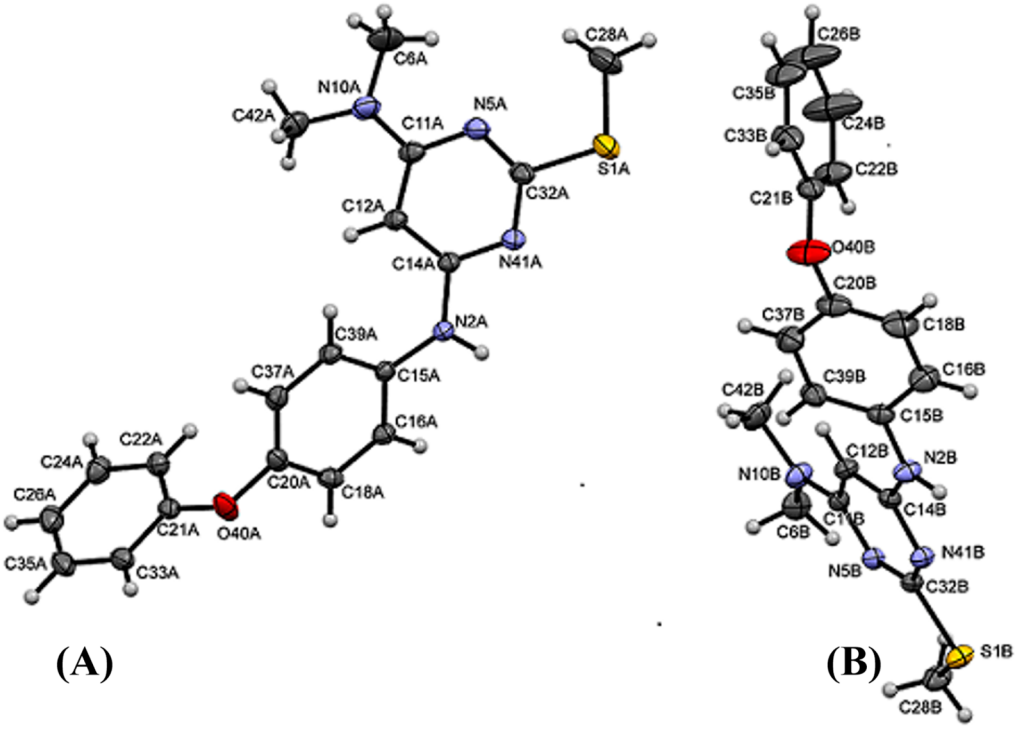

Figure 2. ORTEP view of the asymmetric unit of DMS (A, B) with thermal ellipsoids drawn at 50% probability.

The static second hyperpolarizability and its frequency-dependent counterpart are critical quantities, the average values of which are computed by using specific mathematical expressions.

Since the optical dispersion was not considered here, the static average second hyperpolarizability can be calculated via the Kleinmann expression that is given by

$$\langle\gamma(0;\ 0;\ 0;\ 0)\rangle = \frac{1}{5}\sum_{i,j=x,y,z}(\gamma_{iijj}(0;\ 0;\ 0;\ 0)) \quad \text{for static} \tag{3}$$

$$\langle\gamma(-\omega;\ \omega;\ 0;\ 0)\rangle = \frac{1}{5}\sum_{i,j=x,y,z}(\gamma_{iijj}(-\omega;\ \omega;\ 0;\ 0)) \quad \text{for EOPE} \tag{4}$$

$$\langle\gamma(-2\omega;\ \omega,\ \omega,\ 0)\rangle = \frac{1}{5}\sum_{i,j=x,y,z}(\gamma_{iijj}(-2\omega;\ \omega,\ \omega,\ 0)) \quad \text{for EFSHG} \tag{5}$$

The frequency dependence of the γ-tensor components was omitted to simplify equations 3, (4), and (5).

The average linear polarizability ($\langle\alpha(-\omega;\ \omega)\rangle$) can be related with the linear refractive index ($n(\omega)$) of the crystal by the Clausius-Mossotti relation, which is given by

$$\frac{n(\omega)^2 - 1}{n(\omega)^2 + 2} = \frac{4\pi Z}{3V}\langle\alpha(-\omega;\ \omega)\rangle \tag{6}$$

where Z is the number of molecules in the unit cell and V is the unit cell volume.

The third-order nonlinear susceptibility ($\chi^{(3)}$) is related to the average second hyperpolarizability by the expression

$$\chi^{(3)}(-\omega;\ \omega;\ \omega;\ -\omega) = \left(\frac{(n(\omega)^2 + 2)}{3}\right)^4 \frac{Z}{V}\langle\gamma(-\omega;\ \omega;\ \omega;\ -\omega)\rangle \tag{7}$$

where $\langle\gamma(-\omega;\ \omega;\ \omega;\ -\omega)\rangle$ is the second hyperpolarizability associated with a nonlinear optical process of the intensity-dependent refractive index (IDRI) that is given by the following equation.

$$\langle\gamma(-\omega;\ \omega,\ \omega,\ -\omega)\rangle \cong 2\langle\gamma(-\omega;\ \omega,\ 0,\ 0)\rangle - \langle\gamma(0;\ 0,\ 0,\ 0)\rangle \tag{8}$$

In the context of IDRI, the second hyperpolarizability plays a significant role in determining the material's overall nonlinear optical behavior, which can have important implications for applications in areas such as photonics, telecommunications, and optical signal processing.

2.7.1. The Sum-Over-States (SOS) Method. The sum-over-states (SOS) method, a successful approach in recent years, can calculate the second hyperpolarizability of various organic molecules.[62−68] The SOS method's benefit is its ability to truncate the summation over states for many compounds, as only a few excited states significantly contribute. However, the accuracy of the SOS approach hinges on the theoretical method applied to define the wave functions for ground and excited states and the related excitation energies for dipole moment transitions.

The equations for the second hyperpolarizability using the SOS method is defined as

$$\gamma_{xyzw}(-\omega_s;\ \omega_1,\ \omega_2,\ \omega_3) = \hat{P}[x(-\omega_s),\ y(\omega_1),\ z(\omega_2),\ w(\omega_3)](\Omega_1 - \Omega_2) \tag{9}$$

where

https://doi.org/10.1021/acsomega.3c04380
ACS Omega 2024, 9, 7424−7438

$$\Omega_1 = \sum_{i\neq 0}\sum_{j\neq 0}\sum_{k\neq 0}\left[\frac{\mu_{0i}^{x}\overline{\mu_{ij}^{y}}\,\overline{\mu_{jk}^{z}}\mu_{k0}^{w}}{(\varepsilon_i-\omega_s)(\varepsilon_j-\omega_2-\omega_3)(\varepsilon_k-\omega_3)}\right]$$

$$\Omega_2 = \sum_{i\neq 0}\sum_{j\neq 0}\left[\frac{\mu_{0i}^{x}\mu_{i0}^{y}\mu_{0j}^{z}\mu_{j0}^{w}}{(\varepsilon_i-\omega_s)(\varepsilon_i-\omega_2)(\varepsilon_j-\omega_3)}\right]$$

where $\mu_{ij}^{x} = \langle i|\hat{\mu}^{x}|j\rangle$, $\overline{\mu_{ij}^{x}} = \mu_{ij}^{x} - \mu_{00}^{x}\delta_{ij}$, $\omega_s = \sum_i \omega_i$, and ω is the energy of external fields, $\omega = 0$ corresponds to a static electric field; ε_i stands for excitation energy of state i with respect to ground state 0. $\hat{P}$ is the permutation operator, for γ. μ_{ij}^{x} is the x component of transition dipole moment between state i and j.

All the numerical results for the linear and nonlinear optical parameters were obtained using the Gaussian 16 program package, and the output file was converted to the electronic units (esu).

3. RESULTS AND DISCUSSION

In this section, we will discuss various aspects of DMS properties, covering topics such as its crystal and molecular structure, thermal analysis, molecular reactive properties, density of states, and nonlinear optical properties, ultimately providing a comprehensive understanding of the compound and its potential applications. The rings, C32−N5−C11−C12−C14-N41, C15−C16−C18−C20−C37-C39, and C21−C33−C35−C26−C24-C22, are designed as PhIII, PhII, and PhI, respectively.

3.1. Crystal Structure, Hirshfeld Surface Analysis, and Molecular Structure of DMS. The title compound crystallizes in the monoclinic $P2_1/c$ space group with two molecules in its asymmetric unit (molecules A and B). The major difference between molecules A and B is in their molecular conformations. The dihedral angles between the two aromatic rings are 88.6(8)° and 89.2(1)°, respectively, in A and B molecules. The dihedral angles between the terminal aromatic and pyrimidine rings in A and B molecules are, respectively, 34.5(4)° and 49.6(1)°, while that between central aromatic and pyrimidine rings in A and B are, respectively, 55.0(9)° and 39.6(1)°.

The ORTEP diagram of the compound is given in Figure 2, the crystallographic data and refinement parameters are summarized in Table 1, and the geometric parameters for hydrogen bonds (Å, deg) operating in the crystal structure are listed in Table 2.

The unit cell of the crystal contains 8 molecules of the title compound, 4 molecules of A, and 4 molecules of B. The unit cell contains two c-glide mirrors parallel to the *ac* plane that cut the *b*-axis at $b/4$ and $3b/4$, respectively. Also, the unit cell consists of 2_1 screws parallel to the *b*-axis at $c/4$ and $3c/4$ and repeating itself at a regular distance of $a/2$ along the *a*-axis. The two molecules of A along the *c*-axis (and similarly the two molecules of B along the *c*-axis) are related by one of these c-glides. Each of the two molecular pairs (pair of A molecules and another pair of B molecules), related within the pair by c-glides, creates two respective molecular pairs (a pair of A molecules related by c-glide mirror and another pair containing B molecules also related by a c-glide mirror) through the 2_1-screw axis passing parallel to the *b*-axis at $a/2$. In the crystal, the symmetry-independent A and B molecules are interconnected by N2B−H3B···N41A and N2A−H3A···N41B hydrogen bonds to form a dimer having an $R^2_2(8)$ graph set motif (Figure 3) and which are visualized as intense red spots on d_{norm} mapped surface marked as "a" and "a′" (Figure 4(A)). The arrangements of these hydrogen-bonded A-B pairs in one-half of the unit cell (cut at $c/2$) are exactly opposite to that observed in the other half. The molecular pair are arranged in A···B A···B A···B fashion in one-half of the cell and as B···A B···A B···A in the other half. As there is no further hydrogen bonding between two AB pairs, the supramolecular architecture is zero-dimensional (Figure S6).

The disintegration of 2D-fingerprint depictions of the investigated compound into individual contacts facilitates separation of contributions from each type of contact that otherwise overlap in the full fingerprint plot. The upper spike corresponds to the donor H atom of the N−H group interacting with the N atom of the pyrimidine ring, while the lower spike corresponds to the acceptor N atom of the pyrimidine ring interacting with the H atom of the N−H group. Both look like sharp spikes, which are almost equal in length (highlighted in Figure 4(B), and the N−H/H−N contribution is 10.7%).

For the title compound, the optimized geometrical parameters (bond length (Å), bond angle (deg), dihedral angle (deg)) and their experimental counter values are listed in Table S1. For the title compound, the C−N bond lengths

Table 1. Crystallographic Data and Refinement Parameters of DMS

CCDC number	1909225
Empirical formula	$C_{19}H_{20}N_4OS$
Formula weight	352.45
Temperature/K	296.15
Crystal system	Monoclinic
Space group	$P2_1/c$
a/Å	27.3739(11)
b/Å	14.0483(6)
c/Å	9.7174(4)
α/deg	90
β/deg	90.249(2)
γ/deg	90
Volume/Å^3	3736.9(3)
Z	8
ρ_{calc}g/cm^3	1.253
μ/mm^{-1}	0.187
F(000)	1488.0
Crystal size/mm^3	0.3 × 0.25 × 0.2
Radiation	Mo Kα (λ = 0.71073)
2Θ range for data collection/deg	5.304 to 56.188
Index ranges	$-36 \le h \le 35$, $-18 \le k \le 18$, $-12 \le l \le 12$
Reflections collected	65459
Independent reflections	9053 [R_{int} = 0.0406, R_{sigma} = 0.0261]
Data/restraints/parameters	9053/0/458
Goodness-of-fit on F^2	1.050
Final R indexes [$I \ge 2\sigma(I)$]	R_1 = 0.0518, wR_2 = 0.1424
Final R indexes [all data]	R_1 = 0.0780, wR_2 = 0.1658
Largest diff. peak/hole/e Å^{-3}	0.37/−0.33

Table 2. Geometric Parameters for Hydrogen Bonds (Å, deg) Operating in Crystal Structure of DMS

D-H···A	D-H	H···A	D···A	D-H···A
N2A−H3A···N41B	0.86	2.15	3.0042	177
N2B−H3B···N41A	0.86	2.21	3.0613	174

https://doi.org/10.1021/acsomega.3c04380
ACS Omega 2024, 9, 7424−7438

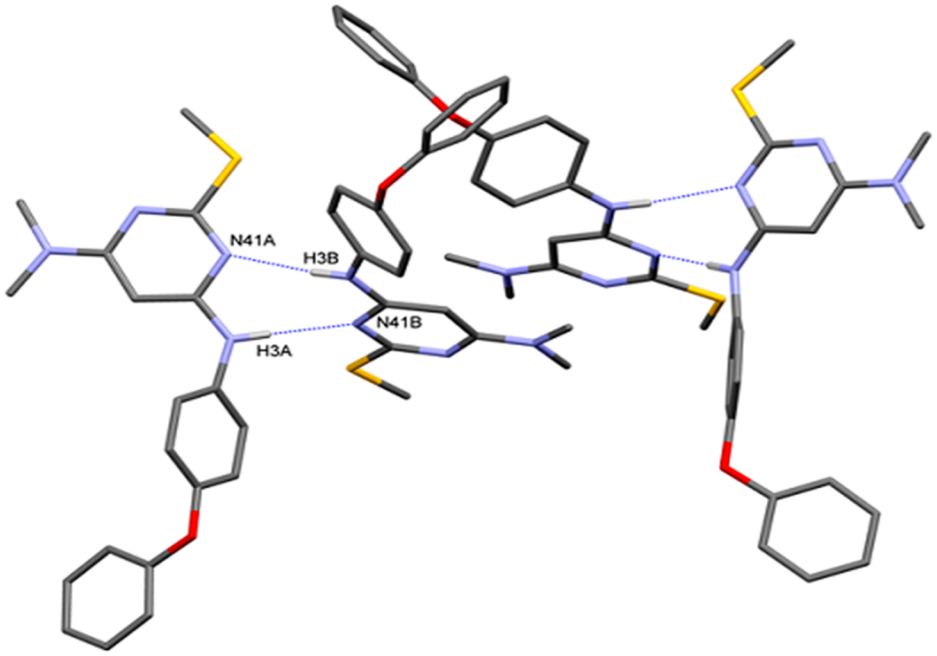

Figure 3. Intermolecular bonds between the A and B molecules.

(DFT/X-ray diffraction (XRD)), namely, C11−N10 (1.37/1.349 Å) and C14−N2 (1.376/1.37 Å), are much shorter than the normal C−N bond length of 1.49 Å[69] but significantly longer than a double bond (1.22 Å), suggesting that these bonds have some multiple bond character.[70] At the N41 position, the C14−N41−C32 angle is decreased by 4.31°, while at the N2 position, the C15−N2−C14 angle is increased by 9.83°. This asymmetry reveals the interaction between the amine and the pyrimidine ring.

3.2. Thermal Analysis. In order to characterize the crystalline structure of DMS, thermogravimetric analysis (TGA)/differential thermal gravimetry (DTG) and differential thermal analysis (DTA) was performed, and the results are shown in Figure 5. From the TGA curve (Figure 5), it can be noted that the compound is stable between 35 and 100 °C. The DMS decomposition occurs in three stages, the first from 100 to 300 °C with mass loss of 4%, followed by a mass loss of 42% from 300 to 373 °C, and finally 30% of the mass is lost in the third stage up 500 °C. The residual mass of the compound was 20%.

The present TGA/DTG study shows that the DMS crystal can be used in optical experiments at temperatures up to 300 °C. Also, the DTA analysis shows an endothermic process at 116 °C with 4.85 μV and 395.49 °C with 57.63 μV (see Figure S7); for greater temperature values, the process is exothermic. From the presented DTG curve, it is possible to identify that the thermal decomposition occurs in the temperature range of 325 to 400 °C.

3.3. Molecular Reactive Properties Studies of DMS. *3.3.1. MEP and ALIE Surfaces.* Local reactive properties of the DMS molecule have been addressed with MEP and ALIE quantum molecular descriptors. Due to their relationship with electronic density, these two descriptors are considered as fundamental quantities.[71−73] The combination of these two descriptors is very useful for the understanding of various reactive properties of the molecules of interest. MEP is closely related to the charge distribution, while ALIE gives information about molecular areas where electrons are least tightly bound. Information provided by MEP and ALIE descriptors are very helpful for the identification of the molecular sites sensitive to electrostatic interactions and to electrophilic attacks.[74] For visualization purposes, it is very convenient to present MEP and ALIE descriptors by mapping their values to the electron density surface, as presented in Figure 6.

Thanks to the combination of MEP and ALIE descriptors, it can be stated that the most reactive locations are the ones located in the vicinity of sulfur and close to a nitrogen atom. Specifically, the MEP surface identifies the location around the sulfur atom as the one with the lowest MEP values, indicating that this part of the molecule might attract positively charged moieties. The other side of the ALIE surface is characterized by the lowest value in the vicinity of nitrogen atom N41, indicating that this molecular location might be the most sensitive location for electrophilic attacks.

3.3.2. Sensitivity toward Autoxidation. It is proven that the autoxidation mechanism is one of the very dangerous factors during the development of new drugs because it is responsible for the formation of potential genotoxic impurities.[75,76] Autoxidation is also very important for predicting the shelf life of organic molecules that are intended to be used as active pharmaceutical components in drug products. In order to estimate the sensitivity of an organic molecule toward autoxidation, it is useful to apply the H-BDE approach.[75−78] The importance of the H-BDE parameter for biochemical processes has also been established in terms of breaking of C−H bonds during phase I drug metabolism.[79] Additionally, one of the most important mechanisms for degradation of organic pollutants, and especially of pharmaceutical molecules, is oxidation.[80] H-BDE values have been calculated in this work in order to evaluate to what extent the DMS molecule could be sensitive toward the autoxidation, and the obtained results are summarized in Figure 7.

It has been established so far that the relevant interval of H-BDE values that indicate sensitivity toward autoxidation is between 70 and 90 kcal/mol.[77,78] Results obtained in this

https://doi.org/10.1021/acsomega.3c04380
ACS Omega 2024, 9, 7424−7438

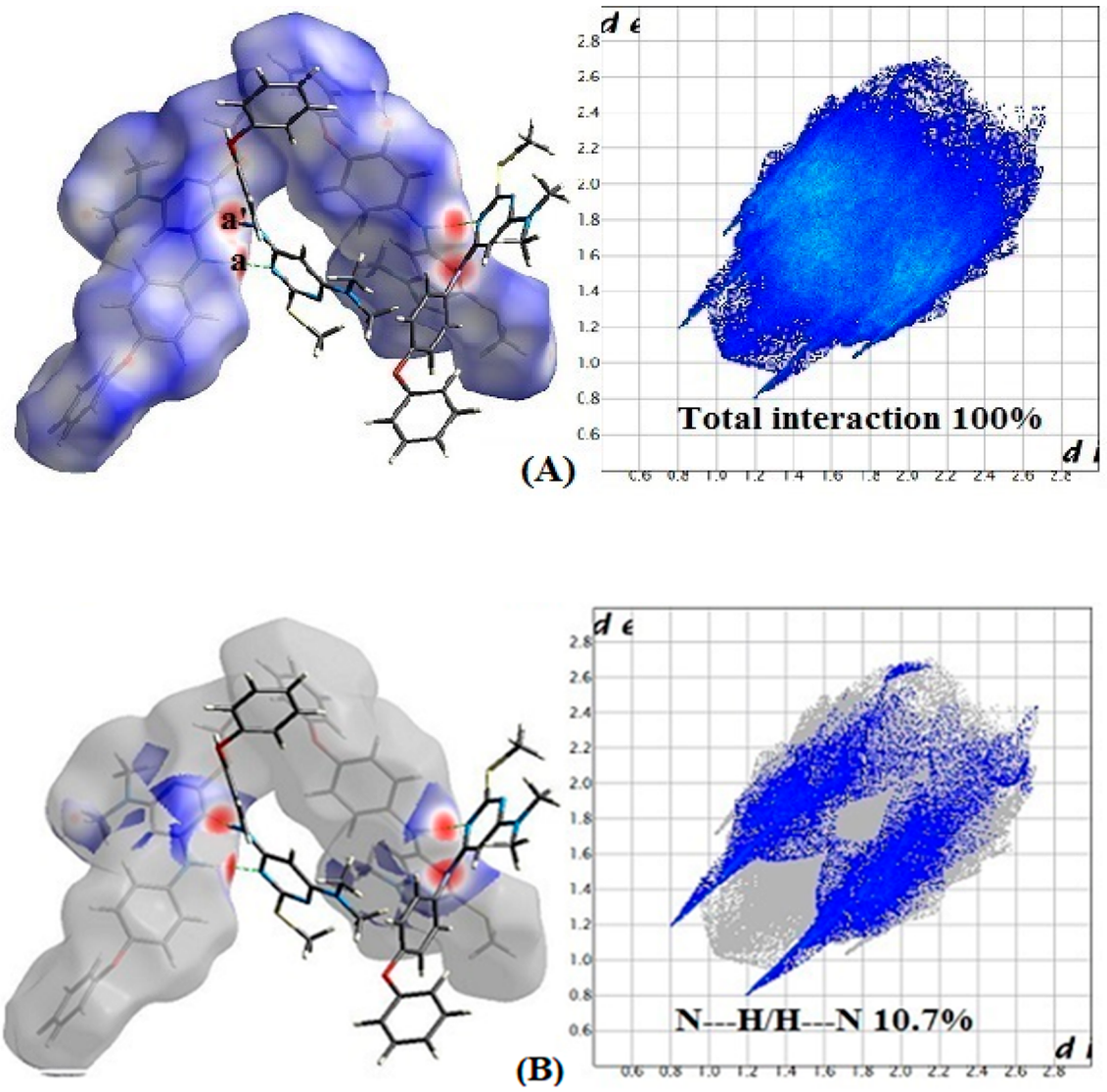

Figure 4. Hirshfeld surface analysis of DMS; (A) Hirshfeld surfaces mapped with d_{norm} showing interactions with neighboring molecules; (B) N−H/H−N contacts on d_{norm} surface with fingerprint plot.

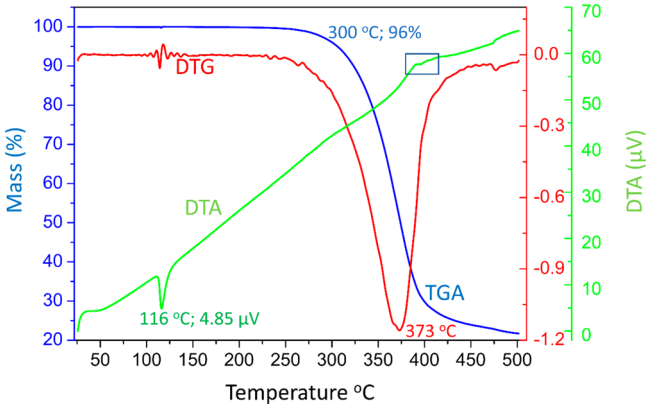

Figure 5. TGA/DTG and DTA data for the DMS compound.

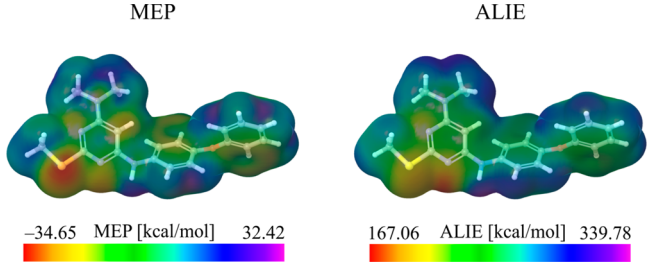

Figure 6. MEP and ALIE surfaces of the DMS molecule.

study for the H-BDE parameter indicate that the DMS molecule has no H-BDE values that would indicate its sensitivity toward the autoxidation mechanism. All H-BDE values are higher than the upper threshold of 90 kcal/mol. The lowest H-BDE values have been calculated for hydrogen atoms of methyl groups and for hydrogen atom H3. This means that the DMS molecule might be highly stable in the presence of oxygen and therefore could have a long shelf life. It also means that its degradation could be difficult under natural conditions, meaning that forced degradation via photocatalysts might be employed for its removal.

3.3.3. Interactions with Water and Determination of Suitable Excipient. The radial distribution function (RDF) is a statistical tool used to analyze the spatial distribution of particles (atoms or molecules) around a reference particle.

https://doi.org/10.1021/acsomega.3c04380
ACS Omega 2024, 9, 7424−7438

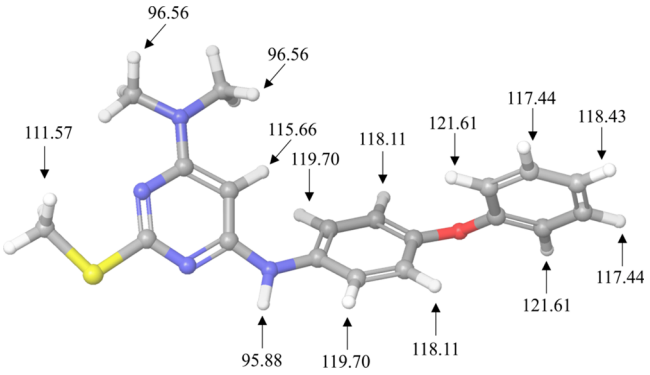

Figure 7. H-BDE values of the DMS molecule.

This tool is especially useful for analyzing the results of MD simulations as it provides information about the probability of finding a surrounding particle at a certain distance from the reference particle. In this regard, RDFs are particularly useful for understanding the interactions and spatial arrangement of molecules in a simulation system.

To evaluate the influence of water molecules on the DMS molecule, we employed the MD simulation on the system containing one DMS molecule surrounded by 2500 water molecules. MD simulation was also performed to estimate which frequently used excipient could be the most suitable for designing practical formulations based on the DMS molecule. For these purposes, MD simulations were performed for the system consisting of 64 DMS molecules.

Analysis of the RDF has been performed to check which atoms of the DMS molecule have the most important interactions with water molecules. RDFs were calculated with respect to the distance between the atom of the DMS molecule and the oxygen atom of water molecules. The most important RDFs indicating relatively significant interactions with water are the ones with sharp peaks on the $g(r)$ vs r curves, which have been presented in Figure 8.

Of all DMS's atoms, only three of them have relatively significant RDF profiles. Although the highest maximal $g(r)$ value has been calculated for carbon atom C6, its peak is located at a very high distance of more than 3.5 Å. Nitrogen atoms N5 and N41 have lower maximal $g(r)$ values, but they are located at significantly lower distances (lower than 3 Å), in comparison with the C6 atom. However, there are no RDFs of hydrogen atoms with maximal $g(r)$ values located at distances lower than 2 Å, which indicates significant interactions with water molecules. Therefore, on account of the MD results, it can be concluded that the DMS molecule has significant stability in water, due to which it could hardly be removed from water resources.

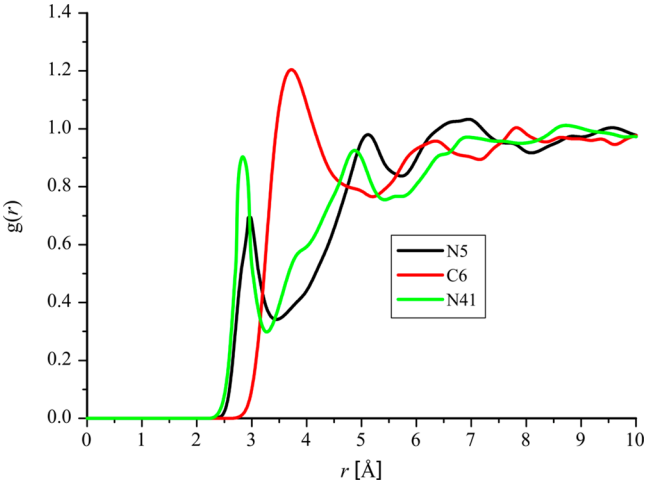

Figure 8. Representative RDFs of the DMS molecule.

The most suitable excipient substance for the DMS molecule was identified by another MD simulation. Excipients are substances that are added to the formulation along with an active component to improve a set of physical and chemical properties such as stabilization, solubility, delivery, etc. Excipients and active components should be compatible, and that compatibility is reflected through similar values of the parameter called solubility parameter.[81−83] This parameter can be calculated by MD simulations according to the following equation

$$\delta = \sqrt{\frac{\Delta H_V - RT}{V_m}} \tag{10}$$

where ΔH_V denotes heat of vaporization, while V_m denotes the molar volume (R is the ideal gas constant, and T the temperature).

Some of the frequently used excipients are polymer polyvinylpyrrolidone (PVP) or sugar molecules such as maltose or sorbitol. In this work, we calculated the solubility parameters of these frequently employed excipients and compared them with the solubility parameter of the DMS molecule. The results are summarized in Table S2.

MD simulation performed on a system containing 64 DMS molecules gave a resulting solubility parameter of 21.192 $MPa^{1/2}$. Results presented in Table S2 indicate that the solubility parameter of the DMS molecule is the closest to the solubility parameter of PVP, a well-known and widely used excipient. This means that PVP could be a suitable excipient for practical formulations based on the DMS molecule.

3.4. Docking Studies. Literature sources indicate that the title compound derivatives extensively showed tank-binding kinase 1 activation. By the docking studies, we want to make lucid whether the title compound can act as useful inhibitors. High-resolution crystal structures of kinase-inhibitor protein reductase were downloaded from the protein data bank (PDB) Web site with PDB identifiers (IDs) 3E5A, 4EUT, and 4EUU.[84,85] Docking was performed using AutoDock 4.2. software.[43] The candidate drug binds at the active and with the aid of weak noncovalent interactions. These results suggest that the title compound might exhibit inhibitory activity against tank-binding kinase.

3.4.1. Interactions between the 3E5A Protein and the DMS Ligand. The interactions between the 3E5A protein and DMS ligand are shown in Figure 9 and tabulated in Table S3.

A conventional hydrogen bond was observed between residue ALA 213 and the ligand's nitrogen atom at a distance of 2.20 Å. Two π-σ interactions involved residues LEU 263 and LEU 139 with the ligand's carbon atom, each at a 3.75 Å distance. Additionally, four alkyl interactions occurred between residues ALA273, LEU 210, VAL147, and ALA160 with the ligand's carbon atom, ranging from 3.02 to 5.36 Å. Lastly, two π-alkyl interactions were present between residues PHE144 and ARG220 with the ligand's carbon atom at distances of 4.06 and 5.12 Å, respectively.

https://doi.org/10.1021/acsomega.3c04380
ACS Omega 2024, 9, 7424−7438

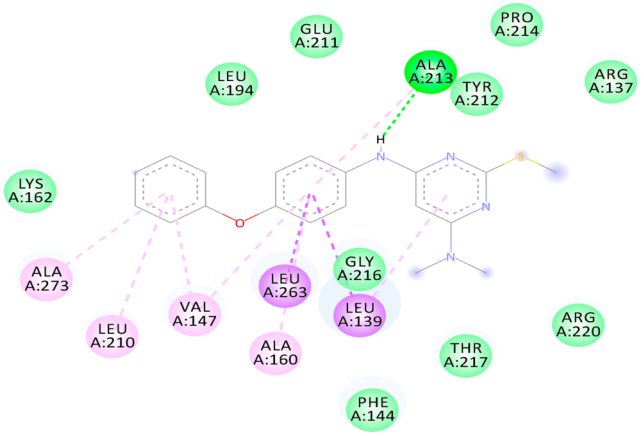

Figure 9. 2D interactions of amino acids of 3E5A with ligand.

3.4.2. Interactions between the 4EUT Protein and DMS Ligand. The interactions between the 3E5A protein and the DMS ligand were shown in Figure 10 and tabulated in Table S3. Two conventional hydrogen bonds involved residues THR20 and ASP157 with the ligand's carbon atoms, ranging from 3.39 to 3.55 Å in distance.

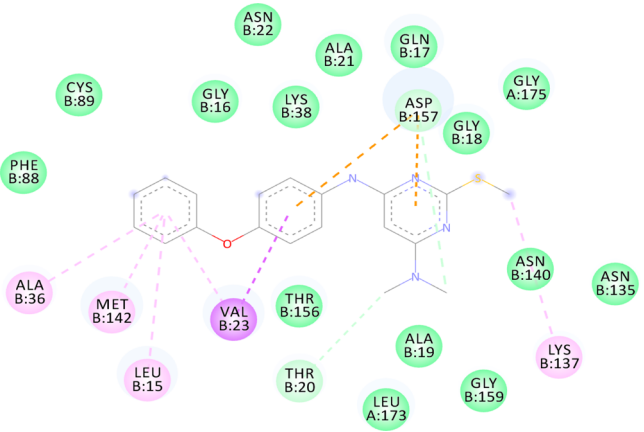

Figure 10. 2D interactions of amino acids of 4EUT with ligand.

Additionally, two π-anion interactions occurred between ASP157 and the ligand's oxygen atoms at distances of 3.32 and 4.56 Å. A single π-σ interaction was observed between residue VAL23 and the ligand's carbon atom at a 3.92 Å distance. Three alkyl interactions took place between residues ALA36, LEU 15, and MET142 with the ligand's carbon atom, ranging from 4.68 to 5.20 Å. Lastly, two π-alkyl interactions were found between residues ALA12, LYS137, and LEU137 with the ligand's carbon atom at distances of 3.966 and 5.00 Å.

3.4.3. Interactions between the 4EUU Protein and DMS Ligand. The interactions between the 4EUU protein and DMS ligand are shown in Figure 11 and tabulated in Table S3. A conventional hydrogen bond was found between residue ASN22 and the ligand at a 3.70 Å distance, while a π-polar hydrogen bond occurred between SER93 and the ligand at a 4.19 Å distance.

Four π-sulfur interactions involved PHE24 and CYS89 with the ligand, ranging from 4.52 to 5.69 Å in distance. Two π-σ interactions were observed between residues TYR95 and MET142 with the ligand's carbon atom, with distances of 3.50 and 5.12 Å, respectively. Three alkyl interactions took place

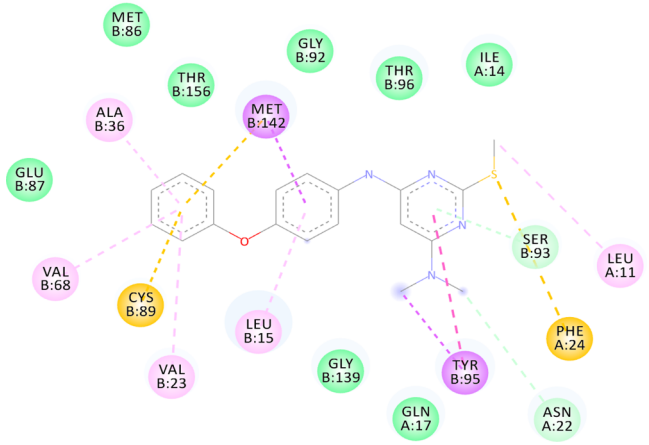

Figure 11. 2D interactions of amino acids of 4EUU with ligand.

between residues VAL26, VAL68, and ALA36 with the ligand's carbon atom, spanning distances from 4.68 to 5.20 Å. Lastly, two π-alkyl interactions were found between residues LEU15 and LEU11 with the ligand's carbon atom at distances of 3.966 and 5.00 Å.

3.5. Density of States of DMS. Identification of the crystal structure of DMS enabled us to perform periodic DFT calculations and to obtain information about the band structure, bandgap, and density of states (DOS). According to our periodic DFT calculations, DMS has an indirect bandgap equal to 3.100 eV. The analysis of the projected density of states (PDOS) enabled us to assess the importance of certain specific atoms of the DMS molecule (Figure 12).

Results presented in Figure 12 denote the contributions of nitrogen, oxygen, and sulfur atoms to the total density of states (TDOS) in the DMS crystal structure. The dotted red line denotes the Fermi level. The valence zone is located in the near vicinity of the red dotted line from the left side, while the conduction zone is located in the near vicinity of the red dotted line from the right side. As indicated in Figure 12a, the highest contribution is from the nitrogen atoms, which clearly contribute mostly to the valence zone of the band structure. Additionally, the nitrogen atoms are also having a relatively important contribution to the conduction zone. The contribution of the nitrogen is followed by that of sulfur, while the lowest contribution has been determined for the oxygen.

3.6. Nonlinear Optical Properties. The Møller−Plesset Perturbation Theory (MP2/6-311+G(d)) was used to calculate the dipole moment and the linear polarizability, and the Density Functional Theory (DFT) at the CAM-B3LYP/6-311+G(d) level was used to calculate the second hyperpolarizability for the DMS isolated and embedded molecules. For the static case, the MP2 results for the components and average values of the electric dipole moment and linear polarizability for both DMS isolated and embedded molecules are shown in Table 3. As can be seen, the environment polarization effects on the dipole moment are strong; the μ-value for the embedded molecule is 2.3 times the value for the isolated molecule, going from 5.22D to 12.04D. This spectacular growth of the crystal dipole moment is mainly due to the increase of the component μ_x, which has the signal for embedded molecule inverted due to the environment polarization effect and results in a growth of the magnitude by more than 58 times. The crystalline polarization effect on the

https://doi.org/10.1021/acsomega.3c04380
ACS Omega 2024, 9, 7424−7438

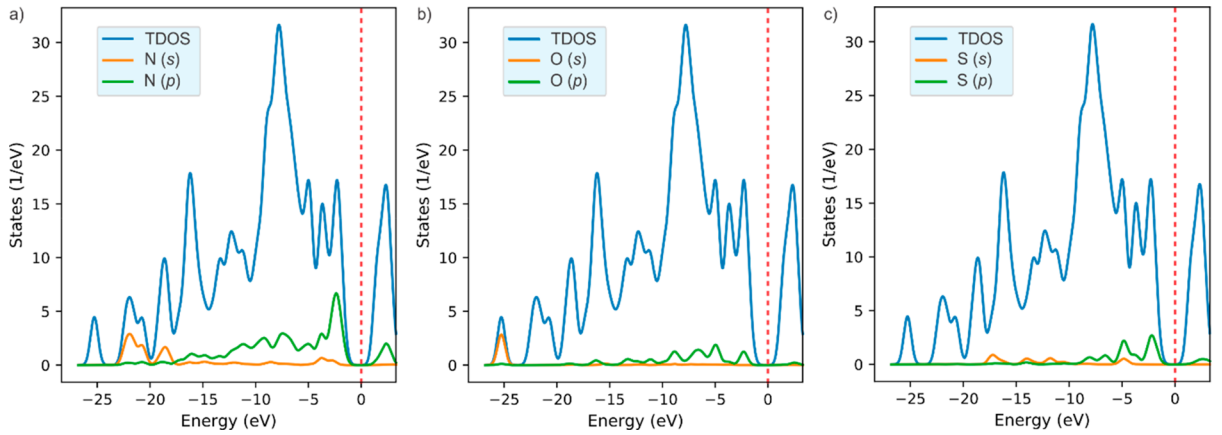

Figure 12. PDOS for (a) nitrogen, (b) oxygen, and (c) sulfur atoms (letters in parentheses denote the *s* or *p* states, the dotted red line indicates the Fermi level).

Table 3. MP2/6-311+G(d) Static Results for the Dipole Moment (μ (D)) and Linear Polarizability ($\alpha(10^{-24}$ esu)) and DFT/CAM-B3LYP/6-311+G(d) Results for the Average Second Hyperpolarizability (γ (10^{-36} esu)) for DMS Isolated and Embedded Molecules

	Isolated	Embedded		Isolated	Embedded		Isolated	Embedded
μ_x	−0.16	9.35	α_{xx}	45.49	45.32	γ_{xxxx}	63.26	118.38
μ_y	5.10	6.57	α_{xy}	−5.78	−5.78	γ_{yyyy}	31.10	169.05
μ_z	1.12	3.77	α_{yy}	39.01	43.59	γ_{zzzz}	25.52	98.06
μ	**5.22**	**12.04**	α_{xz}	13.08	12.74	γ_{xxyy}	15.26	68.06
			α_{yz}	−2.34	−2.48	γ_{yyzz}	9.49	69.25
			α_{zz}	33.58	34.76	γ_{xxzz}	22.81	66.65
			$\langle\alpha\rangle$	**39.36**	**41.23**	$\langle\gamma\rangle$	**42.98**	**158.68**

components μ_y and μ_z present an increase of 29% and 237%, respectively, smaller than that presented by the component μ_x. As can be noted from Table 3, the average linear polarizability ($\langle\alpha\rangle$) presents an increase of 4.75% due to the molecular packing; the diagonal components (α_{ii}) are the ones that are with higher values; and the α_{yy} component presents a greater increase of 11.7% due to the environment polarization.

The DFT/CAM-B3LYP/6-311+G(d) results for the static second hyperpolarizability components (γ_{ijkl}) and the average value ($\langle\gamma\rangle$) for isolated and embedded molecules of DMS are also shown in Table 3. The environment polarization effect on the second hyperpolarizability is very strong, and the $\langle\gamma\rangle$-value of the DMS embedded molecules presents an increase of almost 270% compared to that of an isolated molecule. The magnitude of the static average second hyperpolarizability goes from 42.98 to 158.68 × 10^{-36}.

Figure 13 shows the SOS scheme results for the static average second hyperpolarizability for the DMS isolated molecule as a function of the number of excited states considered in the SOS process. As can be seen, the absolute value of $\langle\gamma(0;0,0,0)\rangle$ is 53.6 × 10^{-36} esu; this value presents an increase of 25.2%, when compared with the value 42.8 × 10^{-36} esu (static).

Figure 14 shows the average linear polarizability ($\langle\alpha(-\omega,\omega)\rangle$) and the average second hyperpolarizability ($\langle\gamma(-\omega;\omega,0,0)\rangle$) as a function of the electric field frequency for the isolated and embedded molecules. As can be seen for the isolated molecule, the dispersion curves for both present a monotonic increase with the increasing of the electric field frequencies; however, for the embedded molecules in the vicinity of the frequencies ω_1 = 0.0428 a.u (λ = 1024 nm) and ω_2 = 0.085 a.u.(λ = 532 nm), the functions show a prominent

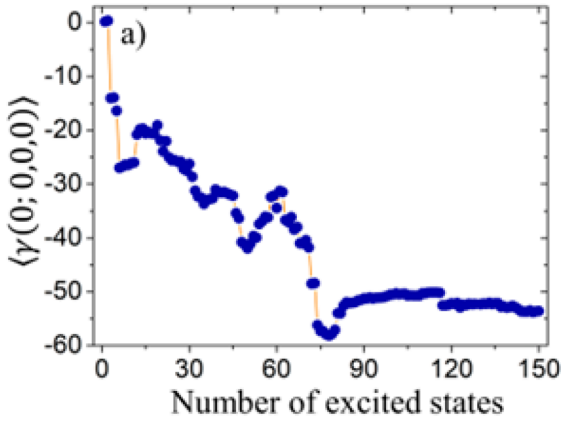

Figure 13. Convergence of the static average second hyperpolarizability ($\langle\gamma(0;0,0,0)\rangle$) calculated via the SOS scheme, in units of 10^{-36} esu, for the DMS isolated molecule.

nonlinear behavior. The $\langle\gamma(-\omega;\omega,0,0)\rangle$ values assume positive and negative values alternately, as can be seen in Figure 14(b) in the intervals; 0.03 < ω < 0.043 a.u, and 0.088 < ω < 0.09 a.u.

Figure 14(c) shows the dispersion relation for $\langle\gamma(-2\omega;\omega,\omega,0)\rangle$ (dc − SHG) (SHG = second harmonic generation) as a function of the applied electric field frequency for DMS isolated and embedded molecules. The $\langle\gamma(-2\omega;\omega,\omega,0)\rangle$ values present a monotonic and smooth increase with an increase in frequency for the DMS isolated molecules. However, the $\langle\gamma(-2\omega;\omega,\omega,0)\rangle$ dispersion relation for DMS embedded molecules presents sharp peaks in the frequency range 0.06 < ω < 0.09 a.u. that clearly can be related to the absorption energies.

https://doi.org/10.1021/acsomega.3c04380
ACS Omega 2024, 9, 7424−7438

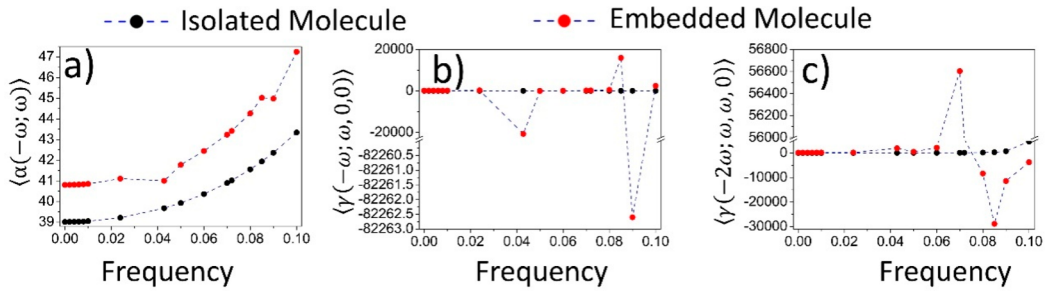

Figure 14. (a) Average linear polarizability $\langle\alpha(-\omega;\omega)\rangle$ and (b) average second hyperpolarizabilities, $\langle\gamma(\omega;\omega,0,0)\rangle$ and (c) $\langle\gamma(-2\omega;\omega,\omega,0)\rangle$, as a function of the electric field frequency for the DMS isolated and embedded molecules.

The analysis of electric charge transfer can be used to explain one of the causes for the nonlinear optical properties of DMS. In Figure S8, we highlight rings A, B, and C, and the details are shown in Table S4. The range of the B-ring charge between 0.139350e and −0.031257e for the isolated and embedded molecules shows a charge transfer due to the effect of the crystalline environment. This negative charge transfer occurs due to the charge transfer from the C and A rings to ring B. Ring A shows a negative electric charge increase of 0.33% over the embedded molecule. On the other hand, when analyzing ring C, an increase of positive electric charge of 112.37% is observed when the isolated molecule is compared with the embedded one.

The findings presented above demonstrate that the DMS compound exhibits resonances near wavelengths of 1064 and 532 nm, indicating that experimental work with this material should steer clear of these frequency regions. As a result, our analysis will focus on the longer wavelength region, exceeding 1064 nm.

Recently, significant efforts have been devoted to identifying organic compounds with large nonresonant, second-order nonlinear responses at the 1907 nm frequency. This interest stems from the fact that *trans*-4-(dimethylamino)-*N*-methyl-4-stilbazolium tosylate (DAST), first reported by Marder et al. in 1989,[86] is a well-established ionic chromophore with second-harmonic generation (SHG) activity and remarkable efficiency at the 1907 nm frequency. Consequently, numerous organic salts (DAST derivatives) with high second-order nonlinearity have been reported, such as DAPSH[87] and DSTMS,[88] which display efficiency similar to or surpassing that of DAST at 1907 nm. In light of this, we will present our findings on the third-order nonlinear optical properties of the DMS crystal at the 1907 nm frequency.[86,89]

To better simulate the crystalline environment, we will consider the entire asymmetric unit of DMS, comprising both molecules A and B as depicted in Figure 3, for constructing the bulk and calculating the NLO properties at 1907 nm. The resonant regions near the frequencies of 1064 and 532 nm were confirmed in both models with a monomer (N = 1) as well as for the dimer (N = 2), both surrounded by point charges. The primary reason for performing calculations with the complete asymmetric unit (dimer) is to evaluate the impact of non-electrostatic interactions on the electric parameters of the DMS crystal. The calculation was carried out by using DFT/CAM-B3LYP/6-311+G(d). Table 4 shows the results of the calculation for the linear and nonlinear optical parameters for embedded DMS in both cases considering the monomer and dimer for construction of the DMS bulk. The dipole moment value for N = 1 (12.02D) presents a reduction of 2.53D (21%) as compared with the result for N = 2 (9.49D); however, the linear polarizability and consequently the linear refractive index present a small increase of ∼2.5%.

Table 4. Results at 1907 nm for μ(D), $\langle\alpha(-\omega,\omega)\rangle$ (10^{-24} esu), $\langle\gamma(-\omega;\omega,0,0)\rangle$ and $\langle\gamma(-\omega;\omega,\omega,-\omega)\rangle$ (10^{-36} esu), and $\chi^{(3)}(-\omega;\omega;\omega;-\omega)$ (10^{-20} m^2/V^2), Divided by N, the Number of Molecules Employed in the SM Simulation

1907 nm		N = 1 (Monomer)	N = 2 (dimer)
μ/N	Isolated	5.22	5.18
	Embedded	12.02	9.49
$\langle\alpha(-\omega,\omega)\rangle/N$	Isolated	39.36	39.33
	Embedded	41.23	42.25
$\langle\gamma(-\omega;\omega,0,0)\rangle/N$	Isolated	44.42	42.84
	Embedded	296.712	3277.22
$\langle\gamma(-\omega;\omega,\omega,-\omega)\rangle/N$	Isolated	45.86	43.99
	Embedded	434.74	6512.71
$\chi^3(-\omega;\omega;\omega\ -\omega)/N$	Isolated	0.78	0.37
	Embedded	7.35	65.41
n	Embedded	1.66	1.68

From Table 4 can be seen that the results of the crystalline environment simulation obtained with the complete asymmetric unit (N = 2) present values of the NLO parameters much greater than the results obtained with only one molecule (N = 1). The second-order hyperpolarizabilities $\langle\gamma(-\omega;\omega,0,0)\rangle$ and $\langle\gamma(-\omega;\omega,\omega,-\omega)\rangle$ per molecule at 1907 nm, 3277.22 × 10^{-36} esu and 6512.71 × 10^{-36} esu, are 11 and 15 times the corresponding value for the monomer, 296.71 × 10^{-36} esu and 434.74 × 10^{-36} esu, respectively. This fact shows that the intermolecular interaction in the asymmetric unit is important and can not be neglected for the DMS bulk construction.

Using equations 5, (6), and (7), we estimated the linear refractive index (n) and the third-order nonlinear susceptibility (χ^3) for the DMS crystal both in the static case and at frequency ω = 0.0239 a.u. (λ = 1907 nm). The obtained results were n = 1.62, χ^3 = 2.96 × 10^{-20} m^2/V^2 (static case) and n = 1.74, χ^3 = 65.41 × 10^{-20} m^2/V^2 (λ = 1907 nm). The $\chi^{(3)}$ value at 1907 nm for the DMS crystal is higher than the values obtained experimentally for five chalcone derivatives,[90−92] as can be seen in Table 5, and qualify the DMS crystal as potential NLO material.

4. CONCLUSION

A potentially new nonlinear optical material, *N*4,*N*4-dimethyl-2-(methylsulfanyl)-*N*6-(4-phenoxyphenyl) pyrimidine-4,6-diamine (DMS) was synthesized, and its structure was experimentally confirmed by single-crystal (SC) XRD, FT-IR,

https://doi.org/10.1021/acsomega.3c04380
ACS Omega 2024, 9, 7424−7438

Table 5. Linear Refractive Index (n) and Third-Order Nonlinear Optical Susceptibility for the DMS Crystal Compared with the Dynamic Experimental Results (ω = 0.086 a.u.) for Some Organic Nonlinear Crystals

	λ (nm)	n	$\chi(3)$ (10^{-20}(-m/V)^2)
DMS (present work)	1907	1.68	65.41
(2E)-3-(3-methylphenyl)-1-(4-nitrophenyl) prop-2-en-1-one (3MPNP)[92]	532	1.418	2.771
1-(5-chlorothiophen-2-yl)-3-(2,3-dimethoxyphenyl)prop-2-en-1-one (CTDMP)[91,92]	532	1.594	0.2383
(2E)-3[4(methylsulfanyl)phenyl] −1-(4-nitrophenyl)prop-2-en-1- one (4N4MSP)[90,92]	800	1.363	0.0237
(2E)-1-(4-bromophenyl)-3-[4(methylsulfanyl)phenyl]prop-2-en-1-one (4Br4MSP)[90,92]	800	1.365	0.0230
(2E)-1-(3-bromophenyl)-3-[4(methylsulfanyl)phenyl]prop-2-en-1-one (3Br4MSP)[90,92]	800	1.360	0.0199

FT-Raman, NMR, and TG/DTA/DTG analysis. The asymmetric unit of DMS consists of a pair of N−H···N hydrogen bonds between the two independent molecules A and B. From the DTA/DTG/TGA analyses, it may be noticed that the investigated compound is stable and could be used in practical applications at temperatures up to 300 °C. High stability of the DMS compound was also confirmed through periodic DFT calculations, which indicated a high value of the bandgap equal to 3.100 eV. Density of states indicated that the nitrogen atoms contribute the most to the reactivity of the studied compound.

The MP2 and DFT/CAM-B3LYP methods, both with the 6-311+G(d) basis set, were used to study the NLO properties of the DMS isolated and embedded molecules. The effects of the crystalline environment polarization on the DMS isolated molecule (or dimer) were simulated by the supermolecule approach (SM/MP2). The static and dynamic electric parameters as the moment dipole and second hyperpolarizabilities were calculated and analyzed. Particularly for the DMS crystal, the obtained result for the third-order nonlinear susceptibility, χ^3 = 65.41 × 10^{-20} m^2/V^2 (λ = 1907 nm), is higher than the values obtained for other organic materials reported in the literature, qualifying the DMS crystal as a potential NLO material to be used in photonic devices fabrication.

Additionally, the molecular properties of DMS were carefully studied. Local reactivity properties were addressed through DFT calculations. MEP surfaces showed that the sulfur atom might attract positively charged moieties. On the other side, ALIE surfaces revealed that the vicinity of nitrogen atom N41 may be possibly sensitive toward electrophilic attacks. All H-BDE values are higher than the upper threshold of 90 kcal/mol, reflecting that the DMS molecule might be highly stable in the presence of oxygen and, therefore, could have a long shelf life without forming the potential genotoxic impurities. Furthermore, molecular dynamic (MD) simulations helped us to identify which atoms of the DMS molecule could have relatively significant interactions with the water molecules. MD simulations also allowed us to calculate the solubility parameter of the title molecule, which turned out to be the closest to the solubility parameter of PVP, a well-known and widely used excipient. Finally, molecular docking studies were performed, and negative binding energies with the ligand were found for three amino acids.

■ ASSOCIATED CONTENT

Supporting Information

The Supporting Information is available free of charge at https://pubs.acs.org/doi/10.1021/acsomega.3c04380.

FTIR spectra, NMR spectra, Hirshfeld surface of DMS, intermolecular bonds between the A and B molecules, highlight of rings A, B, and C with atoms numbered, geometrical parameters of DMS, values of solubility parameter and their differences with respect to DMS molecule, favorable non-bond interaction between DMS and proteins, partial charges in isolated and embedded molecule of DMS (PDF)

■ AUTHOR INFORMATION

Corresponding Authors

Krishna Murthy Potla − *Department of Chemistry, Velagapudi Ramakrishna Siddhartha Engineering College (Autonomous), 520 007 Kanuru, Vijayawada, Andhra Pradesh, India;* orcid.org/0000-0002-5600-1489; Email: krishnamurthypotla@gmail.com

Clodoaldo Valverde − *Laboratório de Modelagem Molecular Aplicada e Simulação (LaMMAS), Campus de Ciências Exatas e Tecnológicas, Universidade Estadual de Goiás, 75001-970 Anápolis, Goiás, Brazil; Universidade Paulista, 74845-090 Goiânia, Goiás, Brazil;* orcid.org/0000-0002-1656-4981; Email: valverde@ueg.br

Authors

Poojith Nuthalapati − *Department of Pharmacology, Sri Ramachandra Institute of Higher Education and Research, 600 116 Ramachandra Nagar, Porur, Chennai, Tamil Nadu, India*

Jahnavi Thokala Sasi Mohan − *Department of General Medicine, Narayana Medical College and Hospital, 524002 Nellore, Andhra Pradesh, India;* orcid.org/0000-0002-3702-4415

Francisco A. P. Osório − *Instituto de Física, Universidade Federal de Goiás, 74690-900 Goiânia, Goiás, Brazil; Pontifícia Universidade Católica de Goiás, 74605-100 Goiânia, Goiás, Brazil*

Suneetha Vankayalapati − *Department of Chemistry, Velagapudi Ramakrishna Siddhartha Engineering College (Autonomous), 520 007 Kanuru, Vijayawada, Andhra Pradesh, India*

Suchetan Parameshwar Adimule − *Department of Studies and Research in Chemistry, University College of Science, Tumkur University, 572 103 Tumkur, Karnataka, India*

Sanja J. Armaković − *Faculty of Sciences, Department of Chemistry, Biochemistry and Environmental Protection, University of Novi Sad, 21000 Novi Sad, Serbia; Association for the International Development of Academic and Scientific Collaboration (AIDASCO), 21000 Novi Sad, Serbia*

Stevan Armaković − *Association for the International Development of Academic and Scientific Collaboration (AIDASCO), 21000 Novi Sad, Serbia; Faculty of Sciences, Department of Physics, University of Novi Sad, 21000 Novi Sad, Serbia*

Y. Sheena Mary − *Department of Physics, FMNC, University of Kerala, 691001 Kollam, Kerala, India*

https://doi.org/10.1021/acsomega.3c04380
ACS Omega 2024, 9, 7424−7438

Complete contact information is available at:
https://pubs.acs.org/10.1021/acsomega.3c04380

Notes

The authors declare no competing financial interest.

■ ACKNOWLEDGMENTS

The author K.M.P. (SQUID-1986-KP-3386) would like to thank the DST/SERB, New Delhi, for financial support (TAR/2021/000275) and also thanks Prof. V.R. Pedireddi, Supramolecular Chemistry Lab, IIT Bhubaneswar, for providing necessary facilities. The authors (S.A. and S.J.A.) acknowledge the financial support of the Ministry of Education, Science and Technological Development of the Republic of Serbia (Grant No. 451-03-47/2023-01/200125). The authors (F.A.P.O. and C.V.) would like to thank the following Brazilian agencies for financial support: Conselho Nacional de Desenvolvimento Científico e Tecnológico (CNPq), Coordenação de Aperfeiçoamento Pessoal de Nível Superior (CAPES); and Fundação de Apoio à Pesquisa do Estado de Goiás (FAPEG). Research developed with support of the High-Performance Computing Center at the UniversidadeEstadual de Goiás (UEG).

■ REFERENCES

(1) Shakir, M.; Singh, B. K.; Kumar, B.; Bhagavannarayana, G. Ferroelectricity in Glycine Picrate: An Astonishing Observation in a Centrosymmetric Crystal. *Appl. Phys. Lett.* **2009**, *95* (25), 252902.
(2) Penn, B. G.; Cardelino, B. H.; Moore, C. E.; Shields, A. W.; Frazier, D. O. Growth of Bulk Single Crystals of Organic Materials for Nonlinear Optical Devices: An Overview. *Prog. Cryst.* **1991**, *22* (1−2), 19−51.
(3) Hadad, C.; Achelle, S.; López-Solera, I.; García-Martínez, J. C.; Rodríguez-López, J. Metal Cation Complexation Studies of 4-Arylvinyl-2,6-Di(Pyridin-2-Yl)Pyrimidines: Effect on the Optical Properties. *Dyes Pigm.* **2013**, *97* (1), 230−237.
(4) Shakir, M.; Bhagavannarayana, G.; Singh, B.; Kumar, B. Organic Ferroelectrics: A Big Surprise. *NPG Asia Mater.* **2010**. DOI: 10.1038/asiamat.2010.48.
(5) Achelle, S.; Ple, N. Pyrimidine Ring as Building Block for the Synthesis of Functionalized π-Conjugated Materials. *Curr. Org. Synth.* **2012**, *9* (2), 163−187.
(6) Achelle, S.; Malval, J.; Aloïse, S.; Barsella, A.; Spangenberg, A.; Mager, L.; Akdas Kilig, H.; Fillaut, J.; Caro, B.; Robin le Guen, F. Synthesis, Photophysics and Nonlinear Optical Properties of Stilbenoid Pyrimidine Based Dyes Bearing Methylenepyran Donor Groups. *ChemPhysChem.* **2013**, *14* (12), 2725−2736.
(7) Fecková, M.; le Poul, P.; Bureš, F.; Robin-le Guen, F.; Achelle, S. Nonlinear Optical Properties of Pyrimidine Chromophores. *Dyes Pigm.* **2020**, *182*, 108659.
(8) Savel, P.; Akdas-Kilig, H.; Malval, J.-P.; Spangenberg, A.; Roisnel, T.; Fillaut, J.-L. Metal-Induced Dimensionality Tuning in a Series of Bipyrimidine-Based Ligands: A Tool to Enhance Two-Photon Absorption. *J. Mater. Chem. C* **2014**, *2* (2), 295−305.
(9) Achelle, S.; Kahlal, S.; Barsella, A.; Saillard, J.-Y.; Che, X.; Vallet, J.; Bureš, F.; Caro, B.; Guen, F. R. Improvement of the Quadratic Non-Linear Optical Properties of Pyrimidine Chromophores by N-Methylation and Tungsten Pentacarbonyl Complexation. *Dyes Pigm.* **2015**, *113*, 562−570.
(10) Boyer, J.; Arnoult, E.; Médebielle, M.; Guillemont, J.; Unge, J.; Jochmans, D. Difluoromethylbenzoxazole Pyrimidine Thioether Derivatives: A Novel Class of Potent Non-Nucleoside HIV-1 Reverse Transcriptase Inhibitors. *J. Med. Chem.* **2011**, *54* (23), 7974−7985.
(11) El-Sayed, W. A.; Rashad, A. E.; Awad, S. M.; Ali, M. M. Synthesis and In Vitro Antitumor Activity of New Substituted Thiopyrimidine Acyclic Nucleosides and Their Thioglycoside Analogs. *Nucleosides Nucleotides Nucleic Acids.* **2009**, *28* (4), 261−274.
(12) Bhatt, J. D.; Chudasama, C. J.; Patel, K. D. Pyrazole Clubbed Triazolo[1,5-a]Pyrimidine Hybrids as an Anti-Tubercular Agents: Synthesis, in Vitro Screening and Molecular Docking Study. *Bioorg. Med. Chem.* **2015**, *23* (24), 7711−7716.
(13) Gregorić, T.; Sedić, M.; Grbčić, P.; Tomljenović Paravić, A.; Kraljević Pavelić, S.; Cetina, M.; Vianello, R.; Raić-Malić, S. Novel Pyrimidine-2,4-Dione-1,2,3-Triazole and Furo[2,3-d]Pyrimidine-2-One-1,2,3-Triazole Hybrids as Potential Anti-Cancer Agents: Synthesis, Computational and X-Ray Analysis and Biological Evaluation. *Eur. J. Med. Chem.* **2017**, *125*, 1247−1267.
(14) Cieplik, J.; Stolarczyk, M.; Pluta, J.; Gubrynowicz, O.; Bryndal, I.; Lis, T.; Mikulewicz, M. Synthesis and antibacterial properties of pyrimidine derivatives. *Acta Pol. Pharm.* **2011**, *68* (1), 57−65.
(15) Alam, O.; Khan, S. A.; Siddiqui, N.; Ahsan, W.; Verma, S. P.; Gilani, S. J. Antihypertensive Activity of Newer 1,4-Dihydro-5-Pyrimidine Carboxamides: Synthesis and Pharmacological Evaluation. *Eur. J. Med. Chem.* **2010**, *45* (11), 5113−5119.
(16) Falcao, E. P. d. S.; de Melo, S. J.; Srivastava, R. M.; Catanho, M. T. J. d. A.; Do Nascimento, S. C. Synthesis and Antiinflammatory Activity of 4-Amino-2-Aryl-5-Cyano-6-{3- and 4-(N-Phthalimidophenyl)} Pyrimidines. *Eur. J. Med. Chem.* **2006**, *41* (2), 276−282.
(17) Singh, K.; Kaur, T. Pyrimidine-Based Antimalarials: Design Strategies and Antiplasmodial Effects. *Med. Chem. Commun.* **2016**, *7* (5), 749−768.
(18) Alam, O.; Mullick, P.; Verma, S. P.; Gilani, S. J.; Khan, S. A.; Siddiqui, N.; Ahsan, W. Synthesis, Anticonvulsant and Toxicity Screening of Newer Pyrimidine Semicarbazone Derivatives. *Eur. J. Med. Chem.* **2010**, *45* (6), 2467−2472.
(19) Vyas, V. S.; Haase, F.; Stegbauer, L.; Savasci, G.; Podjaski, F.; Ochsenfeld, C.; Lotsch, B. V. A Tunable Azine Covalent Organic Framework Platform for Visible Light-Induced Hydrogen Generation. *Nat. Commun.* **2015**, *6* (1), 8508.
(20) Hasanzade, Z.; Raissi, H. Density functional theory calculations and molecular dynamics simulations of the adsorption of ellipticine anticancer drug on graphene oxide surface in aqueous medium as well as under controlled pH conditions. *J. Mol. Liq.* **2018**, *255*, 269−278.
(21) Evans, D. R.; Kwak, H. S.; Giesen, D. J.; Goldberg, A.; Halls, M. D.; Oh-e, M. Estimation of charge carrier mobility in amorphous organic materials using percolation corrected random-walk model. *Org. Electron.* **2016**, *29*, 50−56.
(22) Armaković, S.; Armaković, S. J.; Pelemiš, S.; Mirjanić, D. Influence of sumanene modifications with boron and nitrogen atoms to its hydrogen adsorption properties. *Phys. Chem. Chem. Phys.* **2016**, *18* (4), 2859−2870.
(23) Armaković, S.; Armaković, S. J.; Šetrajčić, J. P.; Holodkov, V. Aromaticity response, and nonlinear optical properties of sumanene modified with boron and nitrogen atoms. *J. Mol. Model.* **2014**, *20* (12), 2538.
(24) Nayak, N.; Prasad, K. S.; Pillai, R. R.; Armakovic, S.; Armakovic, S. J. Remarkable Colorimetric Sensing Behavior of Pyrazole-based Chemosensor Towards Cu(II) Ion Detection: Synthesis, Characterization and Theoretical Investigations. *RSC Adv.* **2018**, *8*, 18023−18029.
(25) Armaković, S.; Armaković, S. J.; Koziel, S. Optoelectronic properties of curved carbon systems. *Carbon.* **2017**, *111*, 371−379.
(26) Vraneš, M.; Armaković, S.; Tot, A.; Papović, S.; Zec, N.; Armaković, S.; Banić, N.; Abramović, B.; Gadžurić, S. Structuring of water in the new generation ionic liquid-Comparative experimental and theoretical study. *J. Chem. Thermodyn.* **2016**, *93*, 164−171.
(27) Bruker. *APEX2*, SADABS, SAINT-Plus, XPREP; Bruker: Madison, WI, 2009.
(28) Sheldrick, G. M. A Short History of *SHELX*. *Acta Crystallogr. A* **2008**, *64* (1), 112−122.
(29) Bochevarov, A. D.; Harder, E.; Hughes, T. F.; Greenwood, J. R.; Braden, D. A.; Philipp, D. M.; Rinaldo, D.; Halls, M. D.; Zhang, J.; Friesner, R. A. Jaguar: A High performance Quantum Chemistry Software Program with Strengths in Life and Materials Sciences. *Int. J. Quantum Chem.* **2013**, *113* (18), 2110−2142.

(30) Shivakumar, D.; Williams, J.; Wu, Y.; Damm, W.; Shelley, J.; Sherman, W. Prediction of Absolute Solvation Free Energies Using Molecular Dynamics Free Energy Perturbation and the OPLS Force Field. *J. Chem. Theory Comput.* **2010**, *6* (5), 1509−1519.
(31) Guo, Z.; Mohanty, U.; Noehre, J.; Sawyer, T. K.; Sherman, W.; Krilov, G. Probing Theα-Helical Structural Stability of Stapled P53 Peptides: Molecular Dynamics Simulations and Analysis. *Chem. Biol. Drug Des.* **2010**, *75* (4), 348−359.
(32) Bowers, K. J.; Sacerdoti, F. D.; Salmon, J. K.; Shan, Y.; Shaw, D. E.; Chow, E.; Xu, H.; Dror, R. O.; Eastwood, M. P.; Gregersen, B. A.; Klepeis, J. L.; Kolossvary, I.; Moraes, M. A. Molecular Dynamics—Scalable Algorithms for Molecular Dynamics Simulations on Commodity Clusters. In *Proceedings of the 2006 ACM/IEEE conference on Supercomputing - SC '06;* ACM Press: New York, New York, USA, 2006; p 84 DOI: 10.1145/1188455.1188544.
(33) *Desmond Molecular Dynamics System;* Schrödinger, LLC: New York, NY, 2021
(34) *Maestro,* Release 2017−4; Schrödinger, LLC: New York, NY, 2017.
(35) Harder, E.; Damm, W.; Maple, J.; Wu, C.; Reboul, M.; Xiang, J. Y.; Wang, L.; Lupyan, D.; Dahlgren, M. K.; Knight, J. L.; Kaus, J. W.; Cerutti, D. S.; Krilov, G.; Jorgensen, W. L.; Abel, R.; Friesner, R. A. OPLS3: A Force Field Providing Broad Coverage of Drug-like Small Molecules and Proteins. *J. Chem. Theory Comput.* **2016**, *12* (1), 281−296.
(36) Jorgensen, W. L.; Maxwell, D. S.; Tirado-Rives, J. Development and Testing of the OPLS All-Atom Force Field on Conformational Energetics and Properties of Organic Liquids. *J. Am. Chem. Soc.* **1996**, *118* (45), 11225−11236.
(37) Jorgensen, W. L.; Tirado-Rives, J. The OPLS [Optimized Potentials for Liquid Simulations] Potential Functions for Proteins, Energy Minimizations for Crystals of Cyclic Peptides and Crambin. *J. Am. Chem. Soc.* **1988**, *110* (6), 1657−1666.
(38) Berendsen, H. J. C.; Postma, J. P. M.; van Gunsteren, W. F.; Hermans, J. Interaction Models for Water in Relation to Protein Hydration. In *Intermolecular Forces. The Jerusalem Symposia on Quantum Chemistry and Biochemistry;* Pullman, B., Ed.; Springer, 1981; Vol. *14*, pp 331−342.
(39) Grimme, S.; Bannwarth, C.; Shushkov, P. A Robust and Accurate Tight-Binding Quantum Chemical Method for Structures, Vibrational Frequencies, and Noncovalent Interactions of Large Molecular Systems Parametrized for All Spd-Block Elements (Z = 1−86). *J. Chem. Theory Comput.* **2017**, *13* (5), 1989−2009.
(40) Bannwarth, C.; Caldeweyher, E.; Ehlert, S.; Hansen, A.; Pracht, P.; Seibert, J.; Spicher, S.; Grimme, S. Extended tight-binding quantum chemistry methods. *WIREs Comput. Mol. Sci.* **2021**, *11* (2), No. e1493, DOI: 10.1002/wcms.1493.
(41) Bannwarth, C.; Ehlert, S.; Grimme, S. GFN2-XTB—An Accurate and Broadly Parametrized Self-Consistent Tight-Binding Quantum Chemical Method with Multipole Electrostatics and Density-Dependent Dispersion Contributions. *J. Chem. Theory Comput.* **2019**, *15* (3), 1652−1671.
(42) Armaković, S.; Armaković, S. J. Atomistica. Online - Web Application for Generating Input Files for ORCA Molecular Modelling Package Made with the Anvil Platform. *Mol. Simul.* **2023**, *49* (1), 117−123.
(43) Morris, G. M.; Huey, R.; Lindstrom, W.; Sanner, M. F.; Belew, R. K.; Goodsell, D. S.; Olson, A. J. Autodock4 and AutoDockTools4: automated docking with selective receptor flexibility. *J. Comput. Chem.* **2009**, *30*, 2785−2791.
(44) Spackman, P. R.; Turner, M. J.; McKinnon, J. J.; Wolff, S. K.; Grimwood, D. J.; Jayatilaka, D.; Spackman, M. A. *CrystalExplorer* : A Program for Hirshfeld Surface Analysis, Visualization and Quantitative Analysis of Molecular Crystals. *J. Appl. Crystallogr.* **2021**, *54* (3), 1006−1011.
(45) Giannozzi, P.; Andreussi, O.; Brumme, T.; Bunau, O.; Buongiorno Nardelli, M.; Calandra, M.; Car, R.; Cavazzoni, C.; Ceresoli, D.; Cococcioni, M.; Colonna, N.; Carnimeo, I.; Dal Corso, A.; de Gironcoli, S.; Delugas, P.; DiStasio, R. A.; Ferretti, A.; Floris, A.; Fratesi, G.; Fugallo, G.; Gebauer, R.; Gerstmann, U.; Giustino, F.; Gorni, T.; Jia, J.; Kawamura, M.; Ko, H.-Y.; Kokalj, A.; Küçükbenli, E.; Lazzeri, M.; Marsili, M.; Marzari, N.; Mauri, F.; Nguyen, N. L.; Nguyen, H.-V.; Otero-de-la-Roza, A.; Paulatto, L.; Poncé, S.; Rocca, D.; Sabatini, R.; Santra, B.; Schlipf, M.; Seitsonen, A. P.; Smogunov, A.; Timrov, I.; Thonhauser, T.; Umari, P.; Vast, N.; Wu, X.; Baroni, S. Advanced Capabilities for Materials Modelling with Quantum ESPRESSO. *J. Phys.: Condens. Matter* **2017**, *29* (46), 465901.
(46) Giannozzi, P.; Baroni, S.; Bonini, N.; Calandra, M.; Car, R.; Cavazzoni, C.; Ceresoli, D.; Chiarotti, G. L.; Cococcioni, M.; Dabo, I.; Dal Corso, A.; de Gironcoli, S.; Fabris, S.; Fratesi, G.; Gebauer, R.; Gerstmann, U.; Gougoussis, C.; Kokalj, A.; Lazzeri, M.; Martin-Samos, L.; Marzari, N.; Mauri, F.; Mazzarello, R.; Paolini, S.; Pasquarello, A.; Paulatto, L.; Sbraccia, C.; Scandolo, S.; Sclauzero, G.; Seitsonen, A. P.; Smogunov, A.; Umari, P.; Wentzcovitch, R. M. QUANTUM ESPRESSO: A Modular and Open-Source Software Project for Quantum Simulations of Materials. *J. Phys.: Condens. Matter* **2009**, *21* (39), 395502.
(47) Perdew, J. P.; Burke, K.; Wang, Y. Generalized Gradient Approximation for the Exchange-Correlation Hole of a Many-Electron System. *Phys. Rev. B* **1996**, *54* (23), 16533−16539.
(48) Valverde, C.; Osório, F. A. P.; Fonseca, T. L.; Baseia, B. DFT Study of Third-Order Nonlinear Susceptibility of a Chalcone Crystal. *Chem. Phys. Lett.* **2018**, *706*, 170−174.
(49) Custodio, J. M. F.; D'Oliveira, G. D. C.; Gotardo, F.; Cocca, L. H. Z.; de Boni, L.; Perez, C. N.; Maia, L. J. Q.; Valverde, C.; Osório, F. A. P.; Napolitano, H. B. Chalcone as Potential Nonlinear Optical Material: A Combined Theoretical, Structural, and Spectroscopic Study. *J. Phys. Chem. C* **2019**, *123* (10), 5931−5941.
(50) Barbosa, M. R.; Costa, I. S. D.; Lopes, T. O.; Valverde, C.; Machado, D. F. S.; Oliveira, H. C. B. de. Theoretical Model of Polarization Effects on Third-Order NLO Properties of the Stilbazolium Derivative Crystal. *J. Phys. Chem. A* **2022**, *126* (48), 8901−8909.
(51) Almeida, L. R.; Anjos, M. M.; Ribeiro, G. C.; Valverde, C.; Machado, D. F. S.; Oliveira, G. R.; Napolitano, H. B.; de Oliveira, H. C. B. Synthesis, Structural Characterization and Computational Study of a Novel Amino Chalcone: A Potential Nonlinear Optical Material. *New J. Chem.* **2017**, *41* (4), 1744−1754.
(52) Valverde, C.; Rodrigues, R. F. N.; Machado, D. F. S.; Baseia, B.; de Oliveira, H. C. B. Effect of the Crystalline Environment on the Third-Order Nonlinear Optical Properties of L-Arginine Phosphate Monohydrate: A Theoretical Study. *J. Mol. Model.* **2017**, *23* (4), 122.
(53) Valverde, C.; Vaz, W. F.; Custodio, J. M. F.; Duarte, V. S.; Carvalho-Jr, P. S.; Figueredo, A. S.; de Aquino, G. L. B.; Baseia, B.; Napolitano, H. B. The Solid State Structure and Environmental Polarization Effect of a Novel Asymmetric Azine. *New J. Chem.* **2017**, *41* (19), 11361−11371.
(54) Vaz, W. F.; Custodio, J. M. F.; Silveira, R. G.; Castro, A. N.; Campos, C. E. M.; Anjos, M. M.; Oliveira, G. R.; Valverde, C.; Baseia, B.; Napolitano, H. B. Synthesis, Characterization, and Third-Order Nonlinear Optical Properties of a New Neolignane Analogue. *RSC Adv.* **2016**, *6* (82), 79215−79227.
(55) Castro, A. N.; Almeida, L. R.; Anjos, M. M.; Oliveira, G. R.; Napolitano, H. B.; Valverde, C.; Baseia, B. Theoretical Study on the Third-Order Nonlinear Optical Properties and Structural Characterization of 3-Acetyl-6-Bromocoumarin. *Chem. Phys. Lett.* **2016**, *653*, 122−130.
(56) Custodio, J. M. F.; Santos, F. G.; Vaz, W. F.; Cunha, C. E. P.; Silveira, R. G.; Anjos, M. M.; Campos, C. E. M.; Oliveira, G. R.; Martins, F. T.; da Silva, C. C.; Valverde, C.; Baseia, B.; Napolitano, H. B. Molecular Structure of Hybrid Imino-Chalcone in the Solid State: X-Ray Diffraction, Spectroscopy Study and Third-Order Nonlinear Optical Properties. *J. Mol. Struct.* **2018**, *1157*, 210−221.
(57) Baseia, B.; Osório, F.; Lima, L.; Valverde, C. Effects of Changing Substituents on the Non-Linear Optical Properties of Two Coumarin Derivatives. *Crystals (Basel).* **2017**, *7* (6), 158.
(58) Poojith, N.; Potla, K. M.; Osório, F. A. P.; Valverde, C.; Vankayalapati, S.; Suchetan, P. A.; Raja, M. Y-Shaped Potential Third-

Order Nonlinear Optical Material - 3-(2-Amino-2-Oxoethyl)-5-Methyl Hexanoic Acid: An Analysis of Structural, Spectroscopic and Docking Studies. *New J. Chem.* **2020**, *44* (42), 18185−18198.
(59) Potla, K. M.; Poojith, N.; Osório, F. A. P.; Valverde, C.; Chinnam, S.; Suchetan, P. A.; Vankayalapati, S. An Analysis of Spectroscopic, Computational and Biological Activity Studies of L-Shaped Sulfamoylbenzoic Acid Derivatives: A Third Order Nonlinear Optical Material. *J. Mol. Struct.* **2020**, *1210*, 128070.
(60) Aguiar, A. S. N.; dos Santos, V. D.; Borges, I. D.; Navarrete, A.; Aguirre, G.; Valverde, C.; Camargo, A. J.; Oliveira, S. S.; Osório, F. A. P.; Fonseca, T. L.; Napolitano, H. B. Bromine Substitution Effect on Structure, Reactivity, and Linear and Third-Order Nonlinear Optical Properties of 2,3-Dimethoxybenzaldehyde. *J. Phys. Chem. A* **2022**, *126* (43), 7852−7863.
(61) Valverde, C.; Vinhal, R. S.; Naves, L. F. N.; Custódio, J. M. F.; Baseia, B.; de Oliveira, H. C. B.; Perez, C. N.; Napolitano, H. B.; Osório, F. A. P. Remarkable Nonlinear Properties of a Novel Quinolidone Derivative: Joint Synthesis and Molecular Modeling. *Molecules.* **2022**, *27* (8), 2379.
(62) Champagne, B.; Kirtman, B. Evaluation of Alternative Sum-over-States Expressions for the First Hyperpolarizability of Push-Pull π-Conjugated Systems. *J. Chem. Phys.* **2006**, *125* (2), 024101.
(63) Pérez-Moreno, J.; Clays, K.; Kuzyk, M. G. A New Dipole-Free Sum-over-States Expression for the Second Hyperpolarizability. *J. Chem. Phys.* **2008**, *128* (8), 084109.
(64) Panja, N.; Ghanty, T. K.; Nandi, P. K. A Sum-over-State Scheme of Analysis of Hyperpolarizabilities and Its Application to Spiroconjugated Molecular System. *Theor. Chem. Acc.* **2010**, *126* (5−6), 323−337.
(65) Coe, J. P.; Paterson, M. J. Approaching Exact Hyperpolarizabilities via Sum-over-States Monte Carlo Configuration Interaction. *J. Chem. Phys.* **2014**, *141* (12), 124118.
(66) Li, W.; Hu, Y.; Zhong, C.; Zhou, X.; Wang, Q.; Tian, W. Q.; Goddard, J. D. The Structural and Photophysical Properties of Multibranched Derivatives with Curved Conjugated Aromatic Cores. *J. Mater. Chem. C* **2016**, *4* (25), 6054−6062.
(67) Tonnelé, C.; Champagne, B.; Muccioli, L.; Castet, F. Second-Order Nonlinear Optical Properties of Stenhouse Photoswitches: Insights from Density Functional Theory. *Phys. Chem. Chem. Phys.* **2018**, *20* (43), 27658−27667.
(68) Rtibi, E.; Abderrabba, M.; Ayadi, S.; Champagne, B. Theoretical Assessment of the Second-Order Nonlinear Optical Responses of Lindqvist-Type Organoimido Polyoxometalates. *Inorg. Chem.* **2019**, *58* (16), 11210−11219.
(69) Poojith, N.; Rani, N. U.; Potla, K. M.; Rose, J. J.; Suchetan, P.A.; Pillai, R. R.; Vankayalapati, S. An analysis of structural, spectroscopic, quantum chemical and in silico studies of ethyl 3-[(pyridin-2-yl)amino]propanoate: A potential thrombin inhibitor. *J. Mol. Struct.* **2021**, *1226*, 129378.
(70) Murthy, P. K.; Sheena Mary, Y.; Shyma Mary, Y.; Panicker, C. Y.; Suneetha, V.; Armakovic, S.; Armakovic, S. J.; Van Alsenoy, C.; Suchetan, P.A. Synthesis, crystal structure analysis, spectral investigations, DFT computations and molecular dynamics and docking study of 4-benzyl-5-oxomorpholine-3-carbamide, a potential bioactive agent. *J. Mol. Struct.* **2017**, *1134*, 25−39.
(71) Politzer, P.; Laurence, P. R.; Jayasuriya, K. Molecular Electrostatic Potentials: An Effective Tool for the Elucidation of Biochemical Phenomena. *Environ. Health Perspect.* **1985**, *61*, 191−202.
(72) Politzer, P.; Murray, J. S. The Fundamental Nature and Role of the Electrostatic Potential in Atoms and Molecules. *Theor. Chem. Acc.* **2002**, *108* (3), 134−142.
(73) Politzer, P.; Murray, J. S.; Bulat, F. A. Average Local Ionization Energy: A Review. *J. Mol. Model.* **2010**, *16* (11), 1731−1742.
(74) Chou, D.; Weinstein, H. Electron Charge Redistribution Following Electrophilic Attack on Heterocycles: Nitrogen as a Charge Transducer. *Tetrahedron.* **1978**, *34* (3), 275−286.
(75) Raillard, S. P.; Bercu, J.; Baertschi, S. W.; Riley, C. M. Prediction of Drug Degradation Pathways Leading to Structural Alerts for Potential Genotoxic Impurities. *Org. Process Res. Dev.* **2010**, *14* (4), 1015−1020.
(76) Lienard, P.; Gavartin, J.; Boccardi, G.; Meunier, M. Predicting Drug Substances Autoxidation. *Pharm. Res.* **2015**, *32* (1), 300−310.
(77) Gryn'ova, G.; Hodgson, J. L.; Coote, M. L. Revising the Mechanism of Polymer Autooxidation. *Org. Biomol. Chem.* **2011**, *9* (2), 480−490.
(78) Wright, J. S.; Shadnia, H.; Chepelev, L. L. Stability of Carbon-Centered Radicals: Effect of Functional Groups on the Energetics of Addition of Molecular Oxygen. *J. Comput. Chem.* **2009**, *30* (7), 1016−1026.
(79) Drew, K. L. M.; Reynisson, J. The Impact of Carbon-Hydrogen Bond Dissociation Energies on the Prediction of the Cytochrome P450 Mediated Major Metabolic Site of Drug-like Compounds. *Eur. J. Med. Chem.* **2012**, *56*, 48−55.
(80) Hovorka, S. W.; Schöneich, C. Oxidative Degradation of Pharmaceuticals: Theory, Mechanisms and Inhibition. *J. Pharm. Sci.* **2001**, *90* (3), 253−269.
(81) Greenhalgh, D. J.; Williams, A. C.; Timmins, P.; York, P. Solubility Parameters as Predictors of Miscibility in Solid Dispersions. *J. Pharm. Sci.* **1999**, *88* (11), 1182−1190.
(82) Rowe, R. C. Adhesion of Film Coatings to Tablet Surfaces —a Theoretical Approach Based on Solubility Parameters. *Int. J. Pharm.* **1988**, *41* (3), 219−222.
(83) Rowe, R. C. Interactions in Coloured Powders and Tablet Formulations: A Theoretical Approach Based on Solubility Parameters. *Int. J. Pharm.* **1989**, *53* (1), 47−51.
(84) Zhao, B.; Smallwood, A.; Yang, J.; Koretke, K.; Nurse, K.; Calamari, A.; Kirkpatrick, R. B.; Lai, Z. Modulation of kinase-inhibitor interactions by auxiliary protein binding: Crystallography studies on Aurora A interactions with VX-680 and with TPX2. *Protein Sci.* **2008**, *17*, 1791−1797.
(85) Ma, X.; Helgason, E.; Phung, Q. T.; Quan, C. L.; Iyer, R. S.; Lee, M. W.; Bowman, K. K.; Starovasnik, M. A.; Dueber, E. C. Molecular basis of tank-binding kinase 1 activation by trans-autophosphorylaton. *Proc. Natl. Acad. Sci. U.S.A.* **2012**, *109*, 9378−9383.
(86) Marder, S. R.; Perry, J. W.; Schaefer, W. P. Synthesis of Organic Salts with Large Second-Order Optical Nonlinearities. *Science.* **1989**, *245* (4918), 626−628.
(87) Figi, H.; Mutter, L.; Hunziker, C.; Jazbinšek, M.; Günter, P.; Coe, B. J. Extremely Large Nonresonant Second-Order Nonlinear Optical Response in Crystals of the Stilbazolium Salt DAPSH. *J. Opt. Soc. Am. B* **2008**, *25* (11), 1786.
(88) Mutter, L.; Brunner, F. D.; Yang, Z.; Jazbinšek, M.; Günter, P. Linear and Nonlinear Optical Properties of the Organic Crystal DSTMS. *J. Opt. Soc. Am. B* **2007**, *24* (9), 2556.
(89) Nakanishi, H.; Oikawa, H. Reprecipitation Method for Organic Nanocrystals. In *Single Organic Nanoparticles;* NanoScience and Technology Book Series; Springer, 2003; pp 17−31. DOI: 10.1007/978-3-642-55545-9_2.
(90) D'silva, E. D.; Podagatlapalli, G. K.; Venugopal Rao, S.; Dharmaprakash, S. M. Study on Third-Order Nonlinear Optical Properties of 4-Methylsulfanyl Chalcone Derivatives Using Picosecond Pulses. *Mater. Res. Bull.* **2012**, *47* (11), 3552−3557.
(91) Prabhu, A. N.; Upadhyaya, V.; Jayarama, A.; Subrahmanya Bhat, K. Synthesis, Growth and Characterization of π Conjugated Organic Nonlinear Optical Chalcone Derivative. *Mater. Chem. Phys.* **2013**, *138* (1), 179−185.
(92) Prabhu, S. R.; Jayarama, A.; Chandrasekharan, K.; Upadhyaya, V.; Ng, S. W. Synthesis, Growth, Structural Characterization, Hirshfeld Analysis and Nonlinear Optical Studies of a Methyl Substituted Chalcone. *J. Mol. Struct.* **2017**, *1136*, 244−252.

https://doi.org/10.1021/acsomega.3c04380
ACS Omega 2024, 9, 7424−7438